TWO-PARTICLE CORRELATIONS IN RELATIVISTIC HEAVY-ION COLLISIONS

Ulrich Heinz

Theory Division, CERN, CH-1211 Geneva 23, Switzerland, ulrich.heinz@cern.ch,
and Institut für Theoretische Physik, Universität Regensburg, D-93040 Regensburg, Germany

Barbara V. Jacak

Department of Physics, SUNY at Stony Brook, Stony Brook, NY 11794, USA,
jacak@skipper.physics.sunysb.edu

ABSTRACT:

Two-particle momentum correlations between pairs of identical particles produced in relativistic heavy-ion reactions can be analyzed to extract the space-time structure of the collision fireball. We review recent progress in the application of this method, based on newly developed theoretical tools and new high-quality data from heavy-ion collision experiments. Implications for our understanding of the collision dynamics and for the search for the quark-gluon plasma are discussed.

CONTENTS

1 INTRODUCTION AND OVERVIEW

1.1 Intensity Interferometry

The method of two-particle intensity interferometry was discovered in the early 1950's by Hanbury Brown and Twiss (HBT) [1] who applied it to the measurement of the angular diameter of stars and other astronomical objects. These first measurements used two-photon correlations. An independent development occurred in the field of particle physics in 1960 by Goldhaber, Goldhaber, Lee and Pais [2] who extracted from two-pion correlations the spatial extent of the annihilation fireball in proton-antiproton reactions. The method exploits the fact that identical particles which sit nearby in phase-space experience quantum statistical effects resulting from the (anti)symmetrization of the multiparticle wave function. For bosons, therefore, the two-particle coincidence rate shows an enhancement at small momentum difference between the particles. The momentum range of this enhancement can be related to the size of the particle source in coordinate space.

HBT interferometry differs from ordinary amplitude interferometry that it compares *intensities* rather than amplitudes at different points. It shows the effects of Bose or Fermi statistics even if the phase of the (light or matter) wave is disturbed by uncontrollable random fluctuations (as is, for example, the case for starlight propagating through the earth's atmosphere) or if the counting rate is very low. To illustrate how the method works and how its applications in astronomy and in particle physics differ let us consider the following simple model [3,4]: two random point sources a and b on a distant emitter, separated by the distance $\boldsymbol{R}$, emit identical particles with identical energies $E_p = (m^2 + p^2)^{1/2}$ which, after travelling a distance L, are measured by two detectors 1 and 2, separated by the distance $\boldsymbol{d}$ (see Figure 1a). L should to be much larger than R or d. The total amplitude measured at detector 1 is then

$$A_1 = \frac{1}{L}\Big(\alpha \, e^{i(pr_{1a}+\phi_a)} + \beta \, e^{i(pr_{1b}+\phi_b)} \Big), \qquad (1)$$

where α, β are the amplitudes emitted by points a and b, ϕ_a, ϕ_b are their random phases, r_{1a}, r_{1b} are their distances to detector 1. The total intensity in 1 is

$$I_1 = \frac{1}{L^2}\Big(|\alpha|^2 + |\beta|^2 + 2\,\mathrm{Re}\,\alpha^* \beta \, e^{i[p(r_{1b}-r_{1a})+(\phi_b-\phi_a)]} \Big), \qquad (2)$$

with a similar result for I_2. The last term in (2) contains information on the distance R between the sources a and b, but it vanishes after averaging the signal
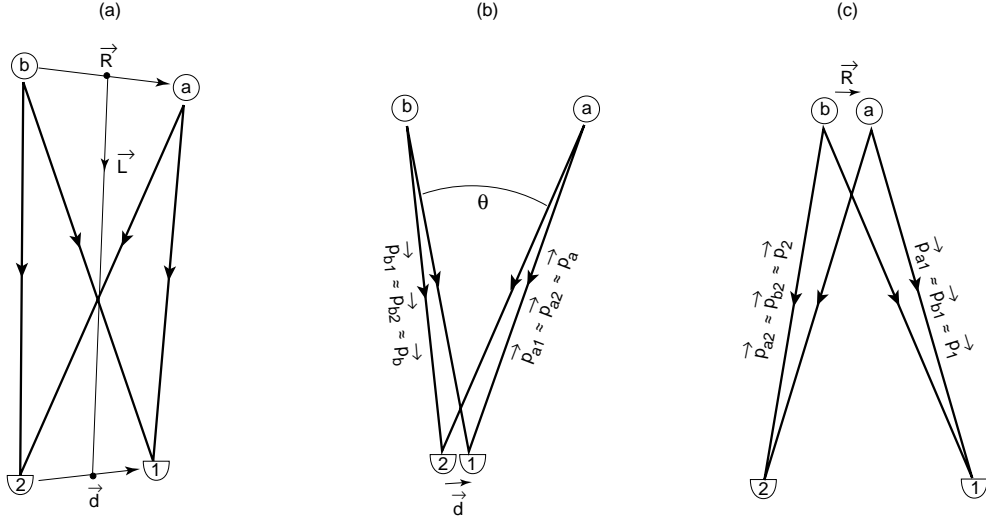
2

Figure 1: Measurement of the separation $\boldsymbol{R}$ of two sources a and b by correlating the intensities in detectors 1 and 2 at varying distances $\boldsymbol{d}$. **a**: The general scheme. **b**: The specific situation in astronomy. **c**: The specific situation in particle physics.

over some time, *i.e.* over the random phases $\phi_{a,b}$:

$$\langle I_1 \rangle = \langle I_2 \rangle = \frac{1}{L^2}\Big(|\alpha|^2 + |\beta|^2\Big). \tag{3}$$

The product of the averaged intensities $\langle I_1 \rangle \langle I_2 \rangle$ is thus independent of both R and d.

The same is not true for the time-averaged *coincidence rate* which is obtained by multiplying the two intensities before averaging:

$$\langle I_1 I_2 \rangle = \langle I_1 \rangle \langle I_2 \rangle + \frac{2}{L^4}|\alpha|^2|\beta|^2 \cos\Big(p(r_{1a} - r_{2a} - r_{1b} + r_{2b})\Big). \tag{4}$$

The two-particle intensity correlation function is thus given by

$$C(\boldsymbol{R}, \boldsymbol{d}) = \frac{\langle I_1 I_2 \rangle}{\langle I_1 \rangle \langle I_2 \rangle} = 1 + \frac{2|\alpha|^2|\beta|^2}{(|\alpha|^2 + |\beta|^2)^2} \cos\Big(p(r_{1a} - r_{2a} - r_{1b} + r_{2b})\Big). \tag{5}$$

For large $L \gg R, d$, the argument of the second, oscillating term becomes

$$r_{1a} - r_{2a} - r_{1b} + r_{2b} \longrightarrow \frac{d\,R}{L}\Big(\cos(\boldsymbol{d}, \boldsymbol{R}) - \cos(\boldsymbol{d}, \boldsymbol{L})\cos(\boldsymbol{R}, \boldsymbol{L})\Big). \tag{6}$$

Note the symmetry of this expression in d and R, the separations of the detectors and of the emitters; this symmetry is lost in the two practically relevant limits:

1. In astronomical applications the emission points a and b are part of a star's surface or of even larger objects, while the detectors on earth are only a few meters or kilometers apart: $R \gg d$. In this limit (see Figure 1b) the cosine-term in (5) reduces to $\cos(\boldsymbol{d}\cdot(\boldsymbol{p}_a - \boldsymbol{p}_b))$, with $\boldsymbol{p}_{a,b} = p\,\boldsymbol{e}_{a,b}$, the unit vectors $\boldsymbol{e}_{a,b}$ giving the directions from the detectors to the two emission points a, b. Experimentally one varies the distance $\boldsymbol{d}$ between the detectors, and from

the resulting oscillation of the signal one extracts the *angular* separation θ of the two emitters via $|\boldsymbol{p}_a - \boldsymbol{p}_b| \sim \theta/\lambda$. Absolute determination of the source separation R is possible only if their distance L is known from elsewhere.

2. In nuclear and particle physics the emitters are very much smaller than the detector separation, $R \ll d$. Then (see Figure 1c) the cosine-term in (5) becomes $\cos(\boldsymbol{R}\cdot(\boldsymbol{p}_1 - \boldsymbol{p}_2))$, in similar notation as above. Now the experimental control variable is the momentum difference $\boldsymbol{p}_1 - \boldsymbol{p}_2$, and $\boldsymbol{R}$ is extracted from the oscillation period.

In real life one has, instead of two discrete ones, a continuum of sources described by a distribution $\rho(\boldsymbol{R})$ of their relative distances. For the case $R \ll d$, after averaging (5) over this relative distance distribution, the measured correlation function is then given by the Fourier transform of $\rho(\boldsymbol{R})$:

$$C(\boldsymbol{p}_1 - \boldsymbol{p}_2) - 1 \sim \int d^3R\, \rho(\boldsymbol{R}) \cos(\boldsymbol{R} \cdot (\boldsymbol{p}_1 - \boldsymbol{p}_2))\,. \tag{7}$$

As we will see, this expression is only applicable to static sources. The assumption of a static source is adequate for stars. The particles emitted in high energy hadron or nuclear reactions, however, come from sources which feature strong dynamical evolution both along the beam direction and transverse to it. As a result, two-particle correlation measurements in heavy-ion physics exhibit a much *richer* structure, but their interpretation is also considerably more involved. The present review covers the technical tools required to access this richness of information and their practical application in heavy-ion reactions.

1.2   HBT Interferometry for Heavy-Ion Collisions

High energy heavy-ion collisions produce hadronic matter under intense conditions of temperature and density. While the highest densities are reached in the early stages of the collision, most of the observed particles are hadrons, which are emitted rather late in the evolution of the collision. For this reason, the measured momentum spectra and correlations contain direct information only about the size, shape, and dynamics of the source at "freeze-out", *i.e.* when the hadrons cease to interact.

The dynamical information is of particular importance as it allows us to connect the observed final state with the hot and dense early stages. Therefore much of the effort in the last few years has gone into the extraction of this dynamics. It turns out that both the single-particle spectra and two-particle correlations are sensitive to certain combinations of thermal and collective motion in the source. A simultaneous analysis of particles with different masses allows for a separation of the two effects: while the thermal motion generates a common momentum distribution in the source, the collective motion creates a flow velocity which combines with the thermal momentum proportionally to the particle's mass. Further discrimination is achieved by combining the spectra with the two-particle correlations which reflect the collective source dynamics through a characteristic momentum dependence of their width parameters.

The aim of HBT (or two-particle Bose-Einstein) interferometry is therefore to provide, in conjunction with a simultaneous analysis of single-particle spectra, a complete and quantitative characterization (both geometrically and dynamically) of the emitting source at "freeze-out". Such a characterization can be used for

backward extrapolations into the interesting dense earlier stages of the collision, and it provides stringent constraints on dynamical models aiming to describe the kinetic evolution of these stages.

1.3 New Developments During the Last Decade

The last decade has brought great strides in measurement, theory, and interpretation of two-particle correlations. Dedicated experiments, optimized for momentum resolution, allow measurement of correlations to very small momentum difference. Much increased statistics of particle pairs has opened the possibility of multidimensional correlation analysis. Correlation functions of identified kaons have become available; as many fewer kaons arise from resonance decays, they provide a more direct picture of the emitting source than the more prevalent pions. Correlations of proton pairs, which will not be discussed here, are also measured in heavy-ion collisions. The experimental programs at the CERN SPS and Brookhaven AGS have allowed comparison between small and large systems at different energies, using S and Pb beams at CERN and lower energy Si and Au beams at the AGS. The comparisons are greatly aided by the development of a commonly accepted analysis formalism among the experiments. Furthermore, the pair momentum dependence of the correlations is now being used to provide dynamical information about the space-time structure of the particle source.

Intensive modeling with event generators, combined with methods to extract correlation functions from them, has been used to study experimental effects such as acceptance and to verify the usefulness of simple model parameterizations in theory. New parametrizations of the two-particle correlation function have been developed which are particularly well adapted for the sources created in high energy collisions. Recently, the necessity of separating geometrical, temporal and dynamical aspects of the correlations has been recognized, and methods to do so have been developed. Intensity interferometry has thus developed into a quantitative tool which at the present stage yields important source parameters at the level of 20% accuracy.

2 THEORETICAL TOOLS FOR ANALYZING TWO-PARTICLE CORRELATIONS

2.1 1- and 2-Particle Spectra and Their Relation to the Emitting Source

The 2-particle correlation function is defined as the ratio of the Lorentz-invariant 2-particle coincidence cross section and the product of the two single particle distributions:

$$C(\boldsymbol{p}_1, \boldsymbol{p}_2) = \frac{E_1 E_2 dN/(d^3 p_1 d^3 p_2)}{(E_1 dN/d^3 p_1)(E_2 dN/d^3 p_2)} \,. \tag{8}$$

The single- and two-particle cross sections are normalized to the average number of particles per event $\langle N \rangle$ and the average number of particles in pairs $\langle N(N-1) \rangle$, respectively. Different normalizations of the correlation function are sometimes used in the literature [5,6]. Careful consideration of the normalization is required when analyzing multi-particle symmetrization effects [7–11].

2.1.1 Pure quantum statistical correlations

The most direct connection between the measured two-particle correlations in momentum space and the source distribution in coordinate space can be established if the particles are emitted independently ("chaotic source") and propagate freely from source to detector. Several approaches to derive this connection [12] are worked out in the literature, parametrizing the source as a covariant superposition of classical currents [5,13–18] or using a superposition of nonrelativistic wave packets [9,10]. One finds the simple relations (with the upper (lower) sign for bosons (fermions))

$$E_p \frac{dN}{d^3p} = \int d^4x \, S(x,p) \,, \tag{9}$$

$$C(\boldsymbol{q},\boldsymbol{K}) = 1 \pm \frac{\left| \int d^4x \, S(x,K) \, e^{iq\cdot x} \right|^2}{\int d^4x \, S(x, K+\tfrac{1}{2}q) \, \int d^4y \, S(y, K-\tfrac{1}{2}q)} \,, \tag{10}$$

where the *emission function $S(x,K)$* is an effective single-particle *Wigner phase-space density* of the particles in the source. (Wigner densities are real but not necessarily everywhere positive.) For the single-particle spectrum (9) this Wigner function must be evaluated on-shell, *i.e.* at $p^0=E_p=(m^2+\boldsymbol{p}^2)^{1/2}$. The correlation function (10) was expressed in terms of the relative momentum $\boldsymbol{q}=\boldsymbol{p}_1-\boldsymbol{p}_2$, $q^0=E_1-E_2$, and average (pair) momentum $\boldsymbol{K}=(\boldsymbol{p}_1+\boldsymbol{p}_2)/2$, $K^0=(E_1+E_2)/2$. As the two measured particles are on-shell, $p^0_{1,2}=E_{1,2}=(m^2+\boldsymbol{p}^2_{1,2})^{1/2}$, the 4-momenta q and K are *off-shell*. They satisfy the orthogonality relation

$$q \cdot K = 0 \,. \tag{11}$$

That on the rhs of Eq. (10) one needs the emission function for off-shell momenta K may at first seem troublesome. In practice, however, the *on-shell approximation $K^0 \approx E_K=(m^2+\boldsymbol{K}^2)^{1/2}$* is very accurate in heavy-ion collisions: the corrections of order $\boldsymbol{q}^2/(8E_K^2)$ are small in the interesting domain of small relative momenta $\boldsymbol{q}$, as a result of the large source sizes and the rest masses of the measured particles. A further simplification is achieved by making in the denominator of (10) the *smoothness approximation* [19,20], taking the product of single-particle spectra at their average momentum $\boldsymbol{K}$:

$$C(\boldsymbol{q},\boldsymbol{K}) \approx 1 \pm \left| \frac{\int d^4x \, S(x,K) \, e^{iq\cdot x}}{\int d^4x \, S(x,K)} \right|^2 \equiv 1 \pm \left| \langle e^{iq\cdot x} \rangle (K) \right|^2 \,. \tag{12}$$

It is exact for exponential single-particle spectra, with corrections proportional to their curvature in logarithmic representation. Both approximations can *a posteriori* be corrected for in the correlation radii ("HBT radii", see below), using information from the measured single-particle spectra [21]. For heavy-ion collisions, such corrections are usually negligible [20,21].

We call $S(x,K)$ an *effective* single-particle Wigner density since different derivations of the relation (10) yield different microscopic interpretations for S. For a detailed discussion of this point we refer to [22]. The differences can become conceptually important in sources with high phase-space density [11]. So far, in heavy-ion collisions the phase-space densities at freeze-out appear to be low enough to neglect them [23,24].

2.1.2   The invertibility problem

The mass-shell constraint (11) eliminates one of the four components of the relative momentum q; for example, it can be resolved as

$$q^0 = \boldsymbol{\beta} \cdot \boldsymbol{q}, \qquad \boldsymbol{\beta} = \boldsymbol{K}/K^0 \approx \boldsymbol{K}/E_K, \tag{13}$$

which gives the energy difference q^0 in terms of $\boldsymbol{q}$ and the velocity $\boldsymbol{\beta}$ of the pair. With only three independent $\boldsymbol{q}$-components, the Fourier transform in (12) cannot be inverted, *i.e.* the space-time structure of $S(x, K)$ cannot be fully recovered from the measured correlator:

$$C(\boldsymbol{q}, \boldsymbol{K}) - 1 \approx \pm \left| \frac{\int_x e^{i\boldsymbol{q} \cdot (\boldsymbol{x} - \boldsymbol{\beta}t)} S(x, K)}{\int_x S(x, K)} \right|^2 = \pm \left| \frac{\int_x e^{i\boldsymbol{q} \cdot \boldsymbol{x}} S(t, \boldsymbol{x} + \boldsymbol{\beta}t; K)}{\int_x S(x, K)} \right|^2. \tag{14}$$

Separation of the spatial and temporal structure of the source thus requires *additional model assumptions* about $S(x, K)$.

We can connect (14) with (7) by introducing the *normalized relative distance distribution* which is a folding of the single-particle emission function with itself:

$$d(x, K) = \int_X s\left(X + \tfrac{x}{2}, K\right) s\left(X - \tfrac{x}{2}, K\right), \quad s(x', K) = \frac{S(x', K)}{\int_{x'} S(x', K)}. \tag{15}$$

d is an even function of x. It allows to rewrite [22] the correlator in the form (7):

$$C(\boldsymbol{q}, \boldsymbol{K}) - 1 \approx \pm \int d^4x \, \cos(q \cdot x) \, d(x, K) = \pm \int d^3x \, \cos(\boldsymbol{q} \cdot \boldsymbol{x}) \, S_{\boldsymbol{K}}(\boldsymbol{x}). \tag{16}$$

In the second equation we used (13) and introduced the *relative source function*

$$S_{\boldsymbol{K}}(\boldsymbol{x}) = \int dt \, d(t, \boldsymbol{x} + \boldsymbol{\beta}t; \boldsymbol{K}, E_K). \tag{17}$$

In the pair rest frame where $\boldsymbol{\beta} = 0$, $S_{\boldsymbol{K}}(\boldsymbol{x})$ is the time integral of the relative distance distribution d, and the time structure of the source is completely integrated out. On the other hand, $S_{\boldsymbol{K}}(\boldsymbol{x})$ is, for each pair momentum $\boldsymbol{K}$, fully reconstructible from the measured correlator $C(\boldsymbol{q}, \boldsymbol{K})$ by inverting the last Fourier transform in (16). This "imaging method" was recently exploited in [25]. As we will see, interesting information about the source dynamics and time structure is then hidden in the $\boldsymbol{K}$-dependence of $S_{\boldsymbol{K}}(\boldsymbol{r})$; the latter can, however, not be unfolded without additional model assumptions about the source.

2.1.3   Final state interactions and unlike particle correlations

HBT measurements in high energy physics are mostly performed with charged particles. These suffer long-range Coulomb repulsion effects on the way from the source to the detector which, even for boson pairs, cause a suppression of the measured correlator at $\boldsymbol{q} = 0$. Moreover, the charged particle pair feels the total electric charge of the source from which it is emitted. Final state effects from strong interactions play a dominant role in proton-proton correlations [26], due to the existence of a strong s-wave resonance in the two-nucleon channel just above threshold. Such final state interaction (FSI) effects are sensitive to the average separation of the two particles at their emission points and thus also contain relevant information about the source size [26, 27, 4].

This has recently led to an increased effort to understand and exploit FSI-induced two-particle correlations which also exist between pairs of *unlike particles* [28–32]. The particular interest in such correlations arises from the fact that, for particles with unequal masses, they allow under certain circumstances to determine the *sign* of the time difference between the emission points of the two particles or the *direction* of their separation at emission [28–32]; this is not possible with correlations between identical particles. In most practical cases, however, the FSI-induced correlations are considerably weaker than the Bose-Einstein correlations between pairs of identical particles.

At the level of accuracy of Eqs. (12,16) which use the smoothness approximation, the correlator can be easily corrected for 2-body final state interactions by replacing $e^{iq \cdot x}$ with a suitable distorted wave. Instead of (16) one thus obtains [26]

$$C(\boldsymbol{q}, \boldsymbol{K}) = \int d^3 r \, S_{\boldsymbol{K}}(\boldsymbol{r}) \left| \Phi_{\boldsymbol{q}/2}(\boldsymbol{r}) \right|^2 . \qquad (18)$$

A slightly more general result which avoids the smoothness approximation was derived in [33]. For simplicity the integral in (18) is written in coordinates of the pair rest frame where $\boldsymbol{K} = 0$. $\Phi_{\boldsymbol{q}/2}(\boldsymbol{r})$ is an FSI distorted scattering wave for the relative motion of the two particles with asymptotic relative momentum $\boldsymbol{q}$; for Coulomb FSI it is given by a confluent hypergeometric function:

$$\Phi_{\boldsymbol{q}/2}^{\text{Coul}}(\boldsymbol{r}) = \Gamma(1 + \eta) \, e^{-\frac{1}{2}\pi\eta} \, e^{\frac{i}{2}\boldsymbol{q}\cdot\boldsymbol{r}} \, F(-i\eta; 1; z_-) , \qquad (19)$$

$$z_{\pm} = \tfrac{1}{2}(qr \pm \boldsymbol{q} \cdot \boldsymbol{r}) = \tfrac{1}{2}qr(1 \pm \cos\theta), \quad \eta = \frac{\alpha \, m}{q}, \qquad (20)$$

where $\alpha = e^2/4\pi$. It describes the propagation of the particle pair from an initial separation $\boldsymbol{r}$ in the pair rest frame, at the time when the second particle was emitted [33], under the influence of the mutual FSI. For identical particle pairs it must be properly symmetrized: $\Phi_{\boldsymbol{q}/2} \mapsto \frac{1}{\sqrt{2}}(\Phi_{\boldsymbol{q}/2} \pm \Phi_{-\boldsymbol{q}/2})$. For a pointlike source $S_{\boldsymbol{K}}(\boldsymbol{x}) = \delta(\boldsymbol{x})$ the correlator (18) with (19) reduces to the Gamov factor $G(\eta)$ (to $2G(\eta)$ for identical particles):

$$G(\eta) = \left| \Gamma(1 + i\eta) e^{-\frac{1}{2}\pi\eta} \right|^2 = \frac{2\pi\eta}{e^{2\pi\eta} - 1} . \qquad (21)$$

For Coulomb FSI it was recently shown [34] that a very good approximation for the Coulomb correction can be taken from *measured* unlike-sign particle pairs in the following form:

$$C_{\text{corr.}}^{\pm\pm}(\boldsymbol{q}, \boldsymbol{K}) = \frac{C_{\text{meas.}}^{+-}(\boldsymbol{q}, \boldsymbol{K}) \, C_{\text{meas}}^{\pm\pm}(\boldsymbol{q}, \boldsymbol{K})}{G(\eta) \, G(-\eta)} . \qquad (22)$$

The denominator (which deviates from unity for small $q \lesssim 8m\alpha$) corrects for the fact that even for a pointlike source the like-sign and unlike-sign Coulomb correlations are not exactly each other's inverse. The important observation in [34] is that this correction is essentially independent of the source size.

The effects of the central charge of the remaining fireball on the charged particle pair were studied in [27, 35]. For a static source it was found that at large pair momenta the FSI reduces (increases) the apparent size (HBT radius) for positively (negatively) charged pairs [27, 35] whereas for small pair momenta the apparent radius increases for both charge states [35]. Expanding sources have not yet been studied in this context, nor has this effect been quantitatively confirmed by experiment. Also, combining the central interaction with two-body FSI remains an unsolved theoretical challenge.

2.2   Source Sizes and Particle Emission Times from HBT Correlations

The two-particle correlation function is usually parametrized by a Gaussian in the relative momentum components. We now discuss different Gaussian parametrizations and establish the relationship of the corresponding width parameters (HBT radii) with the space-time structure of the source.

2.2.1   HBT radii as homogeneity lengths

The space-time interpretation of the HBT radii is based on a Gaussian approximation to the space-time dependence of the emission function $S(x, K)$ [36,21,37–41]. Characterizing the effective source of particles of momentum K by its space-time variances ("rms widths")

$$\langle \tilde{x}_\mu \tilde{x}_\nu \rangle(\boldsymbol{K}) \equiv \langle (x - \bar{x})_\mu (x - \bar{x})_\nu \rangle, \tag{23}$$

where $\langle \ldots \rangle$ denotes the (K-dependent) space-time average over the emission function defined in (12) and $\bar{x}(K) = \langle x \rangle$ is the center of the effective source, one obtains from (12) the following generic Gaussian form for the correlator [36,37,41]:

$$C(\boldsymbol{q}, \boldsymbol{K}) = 1 \pm \exp\left[-q_\mu q_\nu \langle \tilde{x}^\mu \tilde{x}^\nu \rangle(\boldsymbol{K})\right] . \tag{24}$$

This involves the smoothness and on-shell approximations discussed in section 2.1.1 which permit to write the space-time variances $\langle \tilde{x}_\mu \tilde{x}_\nu \rangle$ as functions of $\boldsymbol{K}$ only. Eq. (24) expresses the width of the correlation function in terms of the rms widths of the single-particle Wigner density $S(x, K)$. Note that the absolute space-time position $\bar{x}(\boldsymbol{K})$ of the source center does not appear explicitly and thus cannot be measured.

Instead of the widths of the single-particle function $S(x, K)$ we can also use the widths of the relative distance distribution $d(x, K)$ (see (15)) to characterize the correlation function. Starting from (15) one finds within the same Gaussian approximation $C(\boldsymbol{q}, \boldsymbol{K}) = 1 \pm \exp\left[-\frac{1}{2} q_\mu q_\nu \langle x^\mu x^\nu \rangle_d(\boldsymbol{K})\right]$; here $\langle \ldots \rangle_d$ denotes the average with the relative distance distribution d. Since d is even, $\langle x^\mu \rangle_d \equiv 0$. One sees that the rms widths of S and d are related by a factor 2: $\langle x^\mu x^\nu \rangle_d = 2 \langle \tilde{x}^\mu \tilde{x}^\nu \rangle_S$. This shows that for a Gaussian parametrization of the correlator according to (24), *without a factor $\frac{1}{2}$ in the exponent,* the width parameters are directly related to the rms widths of the single-particle emission function S whereas a similar parametrization *which includes a factor $\frac{1}{2}$ in the exponent* gives as width parameters the rms widths of the relative distance distribution d (or of the relative source function $S_{\boldsymbol{K}}(\boldsymbol{r})$). While the latter interpretation may be mathematically more accurate, the former is more intuitive and has therefore been preferred in the recent literature.

In either case, the two-particle correlator yields *rms widths of the effective source of particles with momentum $\boldsymbol{K}$*. In general, these width parameters do not characterize the total extension of the collision region. They rather measure the size of the system through a filter of wavelength $\boldsymbol{K}$. In the language introduced by Sinyukov [42] this size is the "region of homogeneity", the region from which particle pairs with momentum $\boldsymbol{K}$ are most likely emitted. The space-time variances $\langle \tilde{x}_\mu \tilde{x}_\nu \rangle$ coincide with total source extensions only in the special case that the emission function shows no position-momentum correlations and factorizes, $S(x, K) = f(x)\, g(K)$.

2.2.2   Gaussian parametrizations and interpretation of HBT radii

Relating (24) to experimental data requires first the elimination of one of the four q-components via the mass-shell constraint (11). Depending on the choice of the three independent components different Gaussian parametrizations exist.

A convenient choice of coordinate axes for heavy-ion collisions is the *osl*-system [13, 43], with l denoting the *longitudinal* (or x_l) direction along the beam, o the *outward* (or x_o) direction along the transverse pair momentum vector $\boldsymbol{K}_\perp$, and s the third Cartesian direction, the *sideward* (or x_s) direction. In this system the *sideward* component β_s of the pair velocity $\boldsymbol{\beta}$ in (13) vanishes by definition.

The **Cartesian parametrization** [44] of the correlator (often referred to, historically somewhat incorrectly, as Pratt [13] - Bertsch [43] parametrization) is based on an elimination of q^0 in (24) via (13):

$$C(\boldsymbol{q}, \boldsymbol{K}) = 1 \pm \exp\left(-\sum_{i,j=o,s,l} R_{ij}^2(\boldsymbol{K})\, q_i\, q_j\right). \qquad (25)$$

The Gaussian width parameters (HBT correlation radii) R_{ij} of the Cartesian parametrization are related to the space-time variances of the emission function by [45, 36, 46]

$$R_{ij}^2(\boldsymbol{K}) = \langle (\tilde{x}_i - \beta_i \tilde{t})(\tilde{x}_j - \beta_j \tilde{t}) \rangle, \quad i, j = o, s, l. \qquad (26)$$

These are *6 functions of three variables*: the pair rapidity Y, the modulus $K_\perp$ and the azimuthal angle Φ between the transverse pair momentum $\boldsymbol{K}_\perp$ and the impact parameter $\boldsymbol{b}$. Only these 6 combinations of the 10 independent space-time variances $\langle \tilde{x}_\mu \tilde{x}_\nu \rangle$ can be measured.

For *azimuthally symmetric* collision ensembles the emission function has a reflection symmetry $x_s \to -x_s$, eliminating 3 of the 10 space-time variances, and the correlator is symmetric under $q_s \to -q_s$ [37]. Then $R_{os}^2 = R_{sl}^2 = 0$, and the correlator is fully characterized by *4 functions of only two variables* $K_\perp$ and Y:

$$C(\boldsymbol{q}, \boldsymbol{K}) = 1 \pm \exp\left[-R_s^2 q_s^2 - R_o^2 q_o^2 - R_l^2 q_l^2 - 2R_{ol}^2 q_o q_l\right], \qquad (27)$$

with

$$\begin{aligned} R_s^2(K_\perp, Y) &= \langle \tilde{x}_s^2 \rangle, & R_o^2(K_\perp, Y) &= \langle (\tilde{x}_o - \beta_\perp \tilde{t})^2 \rangle, \\ R_l^2(K_\perp, Y) &= \langle (\tilde{x}_l - \beta_l \tilde{t})^2 \rangle, & R_{ol}^2(K_\perp, Y) &= \langle (\tilde{x}_o - \beta_\perp \tilde{t})(\tilde{x}_l - \beta_l \tilde{t}) \rangle. \end{aligned} \qquad (28)$$

These "HBT radii" mix spatial and temporal information on the source in a non-trivial way, and their interpretation depends on the frame in which the relative momenta q are specified. Extensive discussions of these parameters (including the cross-term R_{ol}^2 which originally appeared in the important, but widely neglected paper [44], was recently rediscovered [36] and then experimentally confirmed [47, 23]) can be found in Refs. [18, 21, 36–41, 52, 48–51]. The cross-term vanishes in any longitudinal reference frame in which the source is symmetric under $x_l \to -x_l$ [44] (e.g. for pion pairs with vanishing rapidity in the center-of-momentum system (CMS) of a symmetric collision); in general it does *not* vanish for pion pairs with non-zero CMS rapidity, not even in the longitudinally co-moving system (LCMS [53]) [48].

For azimuthally symmetric collisions no direction is distinguished for pairs with $K_\perp = 0$. As long as for $K_\perp \to 0$ the emission function reduces to an azimuthally

symmetric expression (an exception is a certain class of opaque source models discussed in section 2.3.4), one has at $K_\perp = 0$ the identities [37] $\langle \tilde{x}_o^2 - \tilde{x}_s^2 \rangle = \langle \tilde{x}_o \tilde{x}_l \rangle = \langle \tilde{t}\tilde{x}_o \rangle = 0$; these imply that $R_o^2 - R_s^2$ and the cross-term R_{ol}^2 vanish at $K_\perp = 0$. At non-zero $K_\perp$ these identities for the space-time variances may be broken by transverse position-momentum correlations in the source, as e.g. generated by transverse collective flow. If the latter are sufficiently weak the leading $K_\perp$-dependence of the difference

$$R_{\text{diff}}^2 \equiv R_o^2 - R_s^2 = \beta_\perp^2 \langle \tilde{t}^2 \rangle - 2\beta_\perp \langle \tilde{x}_o \tilde{t} \rangle + \langle \tilde{x}_o^2 - \tilde{x}_s^2 \rangle \tag{29}$$

is given by the explicit $\beta_\perp$-dependence of the first term on the rhs. This yields the duration of the particle emission process $\Delta t = \sqrt{\langle t^2 \rangle - \langle t \rangle^2}$ for particles with small $K_\perp$ [54, 55, 53]. (This is sometimes loosely called the "lifetime" of the effective source, but should not to be confused with the total time duration between nuclear impact and freeze-out which is not directly measurable.)

The possibility to extract the emission duration from correlation measurements, pointed out by Bertsch and Pratt [54, 55, 53], provided the main motivation for the construction of second generation experiments to measure high quality, high statistics correlation functions. Subsequent model studies for relativistic heavy-ion collisions [56, 52, 57–59] where the emission duration is expected to be relatively short (of the order of the transverse source extension) showed, however, that the extraction of Δt is somewhat model dependent; the relative smallness of the last two terms in (29) cannot always be guaranteed, and their implicit $K_\perp$-dependence can mix with the explicit one of the interesting first term.

The **Yano-Koonin-Podgoretskiĭ (YKP) parametrization** is an alternative Gaussian parametrization of the correlator for *azimuthally symmetric* collisions. It uses the mass-shell constraint (11) to express (24) in terms of $q_\perp = \sqrt{q_o^2 + q_s^2}$, q_l and q^0 [60, 44, 37, 41]:

$$C(\boldsymbol{q}, \boldsymbol{K}) = 1 \pm \exp\left[-R_\perp^2 q_\perp^2 - R_\parallel^2\left(q_l^2 - (q^0)^2\right) - \left(R_0^2 + R_\parallel^2\right)(q \cdot U)^2\right]. \tag{30}$$

Like (27) it has 4 $(K_\perp, Y)$-dependent fit parameters: the three radius parameters $R_\perp(\boldsymbol{K})$, $R_\parallel(\boldsymbol{K})$, $R_0(\boldsymbol{K})$, and a velocity parameter $U(\boldsymbol{K})$ with only a longitudinal spatial component:

$$U(\boldsymbol{K}) = \gamma(\boldsymbol{K})(1, 0, 0, v(\boldsymbol{K})), \qquad \gamma = (1 - v^2)^{-1/2}. \tag{31}$$

The advantage of fitting the form (30) to data is that the extracted YKP radii $R_\perp, R_\parallel, R_0$ do not depend on the longitudinal velocity of the measurement frame, while the fourth fit parameter $v(\boldsymbol{K})$ is simply boosted by that velocity. The frame in which $v(\boldsymbol{K}) = 0$ is called the Yano-Koonin (YK) frame; the YKP radii are most easily interpreted in terms of coordinates measured in this frame [37]:

$$\begin{align}
R_\perp^2(\boldsymbol{K}) &= R_s^2(\boldsymbol{K}) = \langle \tilde{x}_s^2 \rangle, \tag{32} \\
R_\parallel^2(\boldsymbol{K}) &= \langle (\tilde{x}_l - (\beta_l/\beta_\perp)\tilde{x}_o)^2 \rangle - (\beta_l/\beta_\perp)^2 \langle \tilde{x}_s^2 \rangle \approx \langle \tilde{x}_l^2 \rangle, \tag{33} \\
R_0^2(\boldsymbol{K}) &= \langle (\tilde{t} - \tilde{x}_o/\beta_\perp)^2 \rangle - \langle \tilde{x}_s^2 \rangle / \beta_\perp^2 \approx \langle \tilde{t}^2 \rangle, \tag{34}
\end{align}$$

where the approximations in the last two lines are equivalent to dropping the last two terms in (29) (see discussion above). To the extent that these hold, the three YKP radii thus have a straightforward interpretation as the transverse, longitudinal and temporal homogeneity lengths in the YK frame. In particular the time

structure of the source only enters in R_0. For sources with strong longitudinal expansion, like those created in relativistic heavy-ion collisions, it was shown in extensive model studies [41,52,57–59] that the YK velocity $v(\boldsymbol{K})$ very accurately reflects the longitudinal velocity at the center $\bar{x}(\boldsymbol{K})$ of the "homogeneity region" of particles of momentum $\boldsymbol{K}$. The YK frame can thus be interpreted as the rest frame of the effective source of particles with momentum $\boldsymbol{K}$, and the YKP radii measure the transverse, longitudinal and temporal size of this effective source in its own rest frame.

The parametrizations (27) and (30) use different independent components of q but are mathematically equivalent. The YKP parameters can thus be calculated from the Cartesian ones and vice versa [41]. The corresponding relations are

$$R_s^2 \;=\; R_\perp^2\,, \tag{35}$$

$$R_{\text{diff}}^2 \;=\; R_o^2 - R_s^2 = \beta_\perp^2 \gamma^2 \left(R_0^2 + v^2 R_\parallel^2 \right)\,, \tag{36}$$

$$R_l^2 \;=\; \left(1 - \beta_l^2 \right) R_\parallel^2 + \gamma^2 \left(\beta_l - v \right)^2 \left(R_0^2 + R_\parallel^2 \right)\,, \tag{37}$$

$$R_{ol}^2 \;=\; \beta_\perp \left(-\beta_l R_\parallel^2 + \gamma^2 \left(\beta_l - v \right) \left(R_0^2 + R_\parallel^2 \right) \right)\,, \tag{38}$$

whose inversion reads

$$R_\parallel^2 = B - v\,C\,, \qquad R_0^2 = A - v\,C\,, \qquad v = \frac{A+B}{2C} \left(1 - \sqrt{1 - \left(\frac{2C}{A+B} \right)^2} \right)\,, \tag{39}$$

$$A = \frac{1}{\beta_\perp^2}\,R_{\text{diff}}^2\,, \quad B = R_l^2 - 2\frac{\beta_l}{\beta_\perp}\,R_{ol}^2 + \frac{\beta_l^2}{\beta_\perp^2}\,R_{\text{diff}}^2\,, \quad C = -\frac{1}{\beta_\perp}\,R_{ol}^2 + \frac{\beta_l}{\beta_\perp^2}\,R_{\text{diff}}^2\,. \tag{40}$$

These last definitions hold in an arbitrary longitudinal reference frame. According to (39) v is zero in the frame where C vanishes. However, (39) also shows that the YKP parametrization becomes ill-defined if the argument of the square root turns negative. This can indeed happen, in particular for opaque sources [61, 58]; this has motivated the introduction of a *modified YKP parametrization* in [52, 58, 59] which avoids this problem at the expense of a less intuitive interpretation of the modified YKP radii. These remarks show that these relations provide an essential check for the internal consistency of the Gaussian fit to the measured correlation function and for the physical interpretation of the resulting HBT parameters.

2.3 Collective Expansion and $\boldsymbol{K}$-Dependence of the Correlator

If the particle momenta are correlated with their emission points ("x-p-corre-lations"), the space-time variances in (24) depend on the pair momentum $\boldsymbol{K}$. Various mechanisms can lead to such correlations; the most important one for heavy-ion collisions is collective expansion of the source. Recently a major effort has been launched to extract the collective flow pattern at freeze-out from the $\boldsymbol{K}$-dependence of the HBT parameters. However, thermalized sources may exhibit temperature gradients along the freeze-out surface which cause additional x-p-correlations. Moreover, pion spectra receive sizeable contributions from the decay of unstable resonances some time after freeze-out. These decay pions tend to come from a somewhat larger space-time region than the directly emitted ones and, due to the decay kinematics, they preferentially populate the low-momentum region. Together these two effects also generate x-p-correlations for the emitted pions even if the original source did not have them [62].

The separation of these different effects requires extensive model studies some of which will be reviewed below. For didactical reasons we will discuss them in the context of the YKP parametrization where certain mechanisms can be demonstrated most transparently. A translation for the Cartesian fit parameters via the cross-check relations (35)-(38) is straightforward. Furthermore we will show that for sources with strong longitudinal expansion the YK frame (effective source rest frame) is usually rather close to the LCMS (in which the pairs have vanishing longitudinal momentum), *i.e.* $v(\boldsymbol{K}) \approx 0$ in the LCMS. This allows, at least qualitatively, for a rather direct extraction of source properties in its own rest frame from the Cartesian HBT radius parameters in the LCMS. This is important since initially most multi-dimensional HBT analyses were done with the Cartesian parametrization in the LCMS, before the YKP parametrization became popular.

We will concentrate on the discussion of azimuthally symmetric sources (central collisions) for which extensive knowledge, both theoretical and experimental, has been accumulated in the last few years. Many analytical model studies [21,36,37, 39,38,42,40,41,52,48,50,57–59,63,64] are based on the following parametrization of the emission function (or slight variations thereof):

$$S(x,K) = \frac{M_\perp \cosh(\eta - Y)}{8\pi^4 \Delta\tau} \exp\left[-\frac{K \cdot u(x)}{T(x)} - \frac{(\tau - \tau_0)^2}{2(\Delta\tau)^2} - \frac{r^2}{2R^2(\eta)} - \frac{(\eta - \eta_0)^2}{2(\Delta\eta)^2} \right]. \quad (41)$$

Here $r^2 = x^2 + y^2$, $\eta = \frac{1}{2}\ln[(t+z)/(t-z)]$, and $\tau = (t^2 - z^2)^{1/2}$ parametrize the space-time coordinates x^μ, with $d^4x = \tau\, d\tau\, d\eta\, r\, dr\, d\phi$. $Y = \frac{1}{2}\ln[(E_K + K_L)/(E_K - K_L)]$ and $M_\perp = (m^2 + K_\perp^2)^{1/2}$ parametrize the pair momentum $\boldsymbol{K}$. $\sqrt{2}R$ is the 2-dimensional transverse rms radius of the source ($\langle r^2 \rangle = 2R^2$); R is usually taken as a constant. τ_0 is the average freeze-out proper time, $\Delta\tau$ the mean duration of particle emission, and $\Delta\eta$ controls the longitudinal size of the source, $L \sim \tau_0 \sinh\eta$. Note that $S(x,K)$ describes the phase-space distribution at freeze-out and not the dynamical *evolution* of the source from initial conditions; the latter is described by hydrodynamical or microscopic kinetic models, discussed below.

The Boltzmann factor $\exp[-K \cdot u(x)/T(x)]$ parametrizes the momentum-space structure of the source in terms of a collective, directed component, given by a flow velocity field $u^\mu(x)$, and a randomly fluctuating component, characterized by an exponential spectrum with local slope $T(x)$, as suggested by the shape of the measured single-particle spectra. Although this parametrization is somewhat restrictive because it implies that the random component is locally isotropic, it does not *require* thermalization of the source at freeze-out. But if it turns out that all particle species can be described *simultaneously* by the emission function (41), with the *same* temperature and velocity fields $T(x)$, $u(x)$, this would indeed suggest thermalization as the most natural explanation.

It is convenient to decompose $u^\mu(x)$ in the form

$$u^\mu(x) = (\cosh\eta_l \cosh\eta_t,\ \sinh\eta_t\, \boldsymbol{e}_r,\ \sinh\eta_l \cosh\eta_t)\,, \quad (42)$$

with longitudinal and transverse flow rapidities $\eta_l(x)$ and $\eta_t(x)$. A simple boost-invariant longitudinal flow $\eta_l(\tau, \eta, r) = \eta$ ($v_l = z/t$) is commonly assumed. For the transverse flow rapidity profile the simplest choice is

$$\eta_t(\tau, \eta, r) = \eta_f(\tau, \eta) \left(\frac{r}{R(\eta)} \right) \quad (43)$$

with a scale parameter η_f. (In our notation, η_f denotes the transverse collective flow rapidity, whereas $\beta_\perp$ is the transverse velocity of the particle pair.) In most studies η_f was (like R) set constant such that $\eta_t(r)$ was a function of r only. This cannot reproduce the observed rapidity dependence of $\langle p_\perp \rangle$ and of the inverse slopes of the $m_\perp$-spectra [65, 66]. In [63, 64] it was shown that an η-dependence of R, with $R(\eta)$ shrinking in the backward and forward rapidity regions keeping the slope η_f/R in (43) fixed, is sufficient to fully repair this deficiency. Here we discuss only the simpler case of constant R, η_f.

With these assumptions the exponent of the Boltzmann factor in (41) becomes

$$K \cdot u(x) = M_\perp \cosh(Y - \eta) \cosh \eta_t(r) - \boldsymbol{K}_\perp \cdot \boldsymbol{e}_r \sinh \eta_t(r). \qquad (44)$$

For vanishing transverse flow ($\eta_f = 0$) the source depends only on $M_\perp$ and remains azimuthally symmetric for all $K_\perp$. Since in the absence of transverse

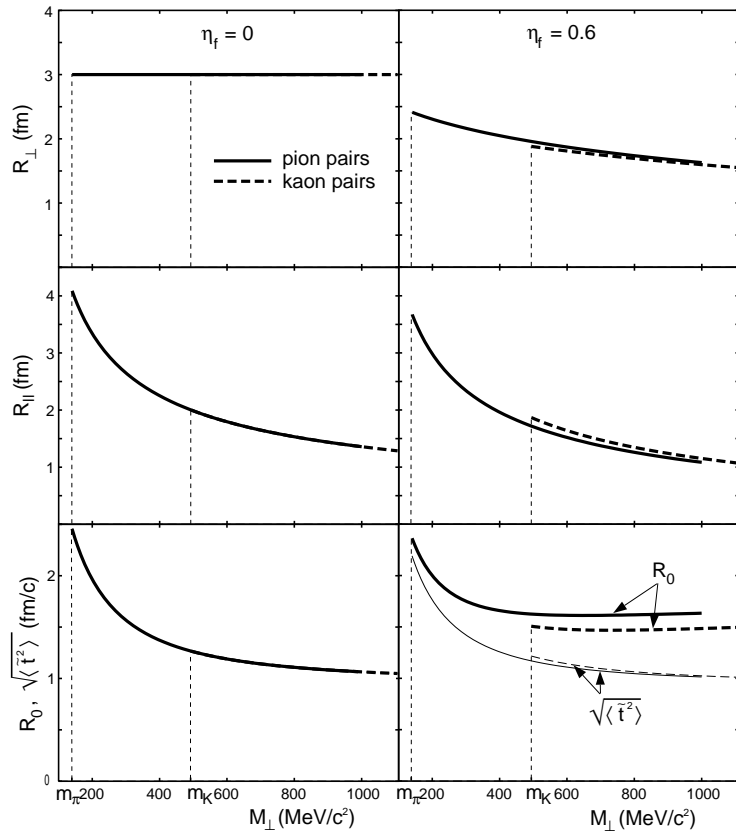Figure 2: The YKP radii $R_\perp$, $R_\parallel$, and R_0 (top to bottom) as functions of $M_\perp$ for pairs at $Y_{\mathrm{cm}} = 0$. Left: no transverse flow. Right: $\eta_f = 0.6$. Solid (dashed) lines are for pions (kaons). Note the breaking of $M_\perp$-scaling by transverse flow. Source parameters: $T = 140$ MeV, $\Delta\eta = 1.2$, $R = 3$ fm, $\tau_0 = 3$ fm/c, $\Delta\tau = 1$ fm/c. (Figure taken from [49].)

flow the β-dependent terms in (33) and (34) vanish and the source itself depends only on $M_\perp$, all three YKP radius parameters then show *perfect $M_\perp$-scaling*: plotted as functions of $M_\perp$, they coincide for pion and kaon pairs (see Figure 2, left column). This remains true if $T(x)$ varies with x; temperature gradients in the source do not destroy the $M_\perp$-scaling.

For $\eta_f \neq 0$ (right column) this $M_\perp$-scaling is broken by two effects: (1) The thermal exponent (44) receives an additional contribution proportional to $K_\perp$. (2) The terms which were neglected in the approximations (33,34) are non-zero, and they also depend on $\beta_\perp = K_\perp/E_K$. Both induce an explicit rest mass dependence and destroy the $M_\perp$-scaling of the YKP size parameters.

2.3.1   Longitudinal flow: Yano-Koonin rapidity and $M_\perp$-dependence of $R_\parallel$

At each point in an expanding source the local velocity distribution is centered around the average fluid velocity $u(x)$. Thus two fluid elements moving rapidly relative to each other are unlikely to contribute particles with small relative momenta. Only source regions moving with velocities close to that of the observed particle pair contribute to the correlation function. How close is controlled by the width of the random component in the momentum distribution: the larger the local "thermal smearing", the more the differences in the fluid velocities can be balanced out, and the larger the "regions of homogeneity" in the source become.

Longitudinal expansion is most clearly reflected in the behaviour of the Yano-Koonin (YK) rapidity $Y_{\mathrm{YK}} = \frac{1}{2}\ln[(1+v)/(1-v)]$. Figure 3 shows (for pion pairs) its dependence on the pair momentum $\boldsymbol{K}$. Transverse flow is seen to have a negligible influence on the YK rapidity. On the other hand, the linear dependence of Y_{YK} on the pair rapidity Y (Figure 3a) is a direct reflection of the longitudinal expansion flow [41]; for a non-expanding source Y_{YK} would be independent of Y. The correlation between the velocities of the pair (Y) and of the emission region (Y_{YK}) strengthens as the thermal smearing decreases. For the Boltzmann form (41) the latter is controlled by $T/M_\perp$, and correspondingly $Y_{\mathrm{YK}}(K_\perp, Y) \to Y$ as $K_\perp \to \infty$. For small $K_\perp$, thermal smearing weakens the correlation, and the effective source moves somewhat more slowly than the observed pairs, whose longitudinal velocities have an additional thermal component.

If the ratio of the longitudinal source velocity gradient to the thermal smearing factor, defined in (46) below, is large, $R_\parallel$ becomes small and the longitudinal rapidity Y_{YK} of the effective source becomes equal to that of the emitted pairs, Y. This can be true even for slow longitudinal expansion as long as it is strong enough compared to the thermal smearing. Consequently, observation of a behaviour like the one shown in Figure 3a demonstrates *strong*, but not necessarily *boost-invariant* longitudinal flow.

Longitudinal expansion is also reflected in the $M_\perp$-dependence of $R_\parallel$ (second row of Figure 2). Comparison of the left with the right diagram shows only minor effects from transverse expansion; longitudinal and transverse dynamics are thus cleanly separated. A qualitative understanding of the $M_\perp$-dependence is provided by the following expression, valid for pairs with $Y = 0$, which can be derived by evaluating (33) via saddle-point integration [67, 21, 38, 39]:

$$R_\parallel^2 \approx L_*^2 \equiv \frac{L_{\mathrm{flow}}^2}{1 + (L_{\mathrm{flow}}/\tau_0 \Delta\eta)^2} \,, \tag{45}$$

$$L_{\mathrm{flow}}(M_\perp) = \frac{1}{\partial \cdot u_l} \sqrt{\frac{T}{M_\perp}} = \tau_0 \sqrt{\frac{T}{M_\perp}} \,, \tag{46}$$

Eq. (46) shows explicitly the competition between the longitudinal velocity gradient $\partial \cdot u_l$ and the thermal smearing factor $T/M_\perp$. For *strong* longitudinal expansion (large velocity gradient and/or weak thermal smearing) and/or large

geometric longitudinal extension $\tau_0 \Delta\eta$ of the source the second term in the denominator can be neglected, and $R_\parallel$ drops steeply as $1/\sqrt{M_\perp}$ [67]. Note that quantitative corrections to (45) are not always small [40].

We emphasize that only the first equation in (46) is general. The appearance of the parameter τ_0 in the second equation is due to the choice of a Bjorken profile for the longitudinal flow for which the longitudinal velocity gradient is given by the total proper time τ_0 between impact and freeze-out. This is not true in general; the interpretation of the length $R_\parallel$ in terms of the total expansion time is therefore a highly model-dependent procedure which should be avoided. As a matter of principle, the absolute temporal position of the freeze-out point is not measurable, see section 2.2.1.
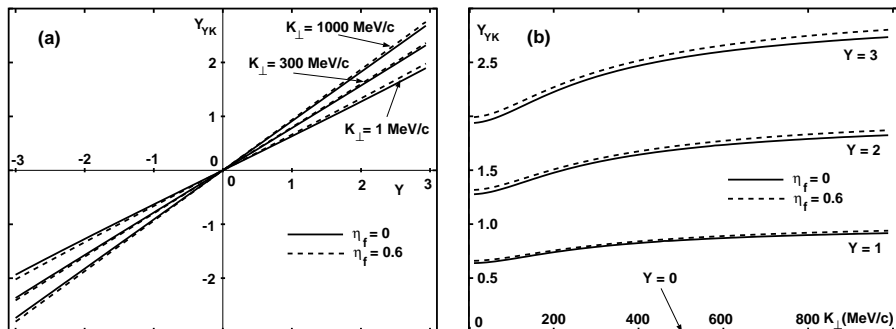

Figure 3: (a) The Yano-Koonin rapidity for pion pairs, as a function of the pair c.m. rapidity Y, for various values of $K_\perp$ and two values for the transverse flow η_f. (b) The same, but plotted against $K_\perp$ for various values of Y and η_f. Source parameters as in Fig. 2. (Figure taken from [41].)

Strong longitudinal x-p-correlations also occur in string fragmentation. In fact, in the Schwinger model of string breaking [68] the quark pairs created from the chromoelectric field are assumed to have longitudinal momentum $Y = \eta$, without thermal fluctuations. Thus a similar linear rise of the YK-rapidity with the pair rapidity and a strong decrease of $R_\parallel(M_\perp)$ would also be expected in jet fragmentation (with the x_l-axis oriented along the jet axis). It would be interesting to confirm this prediction [57] in e^+e^- or pp collisions.

2.3.2   Transverse flow: $M_\perp$-dependence of $R_\perp$

Just as longitudinal expansion affects $R_\parallel$, transverse flow causes an $M_\perp$-dependence of $R_\perp$. This is seen in the first row of diagrams in Figure 2, which also shows that longitudinal flow does not contribute to this feature: for $\eta_f = 0$ the transverse radius does not depend on $M_\perp$, in spite of strong longitudinal expansion of the source. A qualitative understanding of this behaviour is given by the analogue of (45), again obtained by evaluating (32) via saddle point integration [21, 39, 37]:

$$R_\perp^2 \approx R_*^2 \equiv \frac{R^2}{1 + (R/R_{\text{flow}})^2} = \frac{R^2}{1 + \eta_f^2 (M_\perp/T)}, \tag{47}$$

$$R_{\text{flow}}(M_\perp) = \frac{1}{\partial\eta_t(r)/\partial r} \sqrt{\frac{T}{M_\perp}} = \frac{R}{\eta_f} \sqrt{\frac{T}{M_\perp}}. \tag{48}$$

Once again there is competition between flow velocity gradients in the source, this time in the transverse direction, which tend to reduce the homogeneity regions, and thermal smearing by the factor $T/M_\perp$ resulting from the random component in the momentum distribution, enlarging the regions of homogeneity. The left equations in (47,48) are generic while the right ones apply to the specific transverse flow profile (43).

Transverse flow must be built up from zero during the collision while longitudinal x-p-correlations may contain a sizeable primordial component from incomplete stopping of the two nuclei and/or the particle production process (e.g. string fragmentation, see above). One thus expects generically weaker transverse than longitudinal flow effects at freeze-out. Correspondingly, in realistic simulations (e.g. [39, 57, 56]) the longitudinal homogeneity length $R_\parallel$ turns out to be dominated by the expansion (*i.e.* by L_{flow}) while in the transverse direction the geometric size R dominates at small $M_\perp$, with flow effects taking over only at larger values of $M_\perp$. Correspondingly, $R_\perp(M_\perp)$ decreases more slowly at small $M_\perp$ than $R_\parallel(M_\perp)$ [40, 57].

2.3.3   The emission duration

Saddle-point integration of (34) with the source (41) yields, with L_* from (45),

$$R_0^2 \approx (\Delta t_*)^2 \equiv (\Delta\tau)^2 + 2\left(\sqrt{\tau_0^2 + L_*^2} - \tau_0\right)^2. \qquad (49)$$

The $M_\perp$-dependence of L_* thus induces an $M_\perp$-dependence of the temporal YKP parameter. Eq. (49) reflects the proper time freeze-out assumed in the model (41): particles emitted at different points z are also emitted at different global times t, and the total temporal width of the effective source is thus given by the Gaussian width $\Delta\tau$ plus the additional variation along the proper time hyperbola, integrated over the longitudinal homogeneity region L_* [40].

Although (49) suggests that the proper emission duration $\Delta\tau$ can be measured via R_0 in the limit $M_\perp \to \infty$ (where $L_* \to 0$), this is has not been true in systems studied to date. For transversely expanding sources R_0 receives additional contributions from the $\beta_\perp$-dependent terms in (34), in particular at large $M_\perp$ (see Figure 2). The most important correction is due to the term $\langle \tilde{x}_o^2 - \tilde{x}_s^2 \rangle / \beta_\perp^2$ which can have either sign and usually grows with $M_\perp$ [57, 59, 61]. The extraction of the emission duration must thus be considered the most model-dependent aspect of the HBT analysis.

2.3.4   Temperature gradients and opacity effects

A different source of transverse x-p-correlations which can compete with transverse flow in generating an $M_\perp$-dependence of $R_\perp$ are transverse temperature gradients in the emission function. Since particle densities and mean free paths (which control the freeze-out process [69, 70]) depend very strongly on temperature, one would *a priori* not expect strong temperature variations across the freeze-out surface [71]. While transverse temperature gradients and transverse flow affect $R_\perp$ similarly (except that the latter weakly breaks the $M_\perp$-scaling), they have quite different effects on the single particle spectra [39, 50]: transverse temperature gradients strongly reduce the flattening effect of transverse flow on the $m_\perp$-spectra which is needed to reproduce the data [70, 72]. Thus constrained

by single-particle data, their phenomenological usefulness is limited. Temporal temperature gradients only reduce the emission duration, but do not affect the transverse R-parameter [39, 50].

One possible source feature that parametrization (41) cannot describe is "opacity", *i.e.* surface dominated emission. Heiselberg and Vischer generated opaque sources by multiplying (41) (or a similar source with bulk freeze-out) with an exponential absorption factor [61] (see also [58])

$$S_{\mathrm{opaque}}(x, p) \;=\; S(x, p) \exp\left[-\sqrt{8/\pi}\,(l_{\mathrm{eff}}/\lambda_{\mathrm{mfp}}) \right], \qquad (50)$$

$$l_{\mathrm{eff}} \;=\; l_{\mathrm{eff}}(r, \phi) = e^{-\frac{x_s^2}{2R^2}} \int_{x_o}^{\infty} e^{-\frac{x'^2}{2R^2}}\, dx' . \qquad (51)$$

The ratio λ_{mfp}/R controls the degree of opacity of the source; as $\lambda_{\mathrm{mfp}}/R \to 0$, the source becomes an infinitely thin radiating shell. The parametrization (50) together with (41) leads to sources with negative $\langle \tilde{x}_o^2 - \tilde{x}_s^2 \rangle$ *for all values* of $K_\perp$ (including the limit $K_\perp \to 0$). According to (29) and (34) this leads to negative values of R_{diff}^2 and R_0^2 (R_0^2 even diverges as $K_\perp \to 0$ [58]); the data (see below) are consistent with vanishing or positive R_{diff}^2 at small $K_\perp$.

A non-vanishing difference $\langle \tilde{x}_o^2 - \tilde{x}_s^2 \rangle$ in the limit $K_\perp \to 0$ violates the postulated azimuthal symmetry of the source (see discussion before Eq. (29)). It is easy to see that short-lived sources can never be opaque for particles with $K_\perp \to 0$: the source shrinks to zero before such particles can be reabsorbed. The particular behaviour excluded in [58] is thus anyhow rather unphysical. At larger $K_\perp$, on the other hand, the "opacity signal" $\langle \tilde{x}_o^2 - \tilde{x}_s^2 \rangle < 0$ (leading, if strong enough, to $R_o^2 < R_s^2$ [61]) can be "faked" by other mechanisms: Tomášik found [52, 59] that expanding sources with a box-like transverse density profile generate exactly such a signature. At the moment it is thus unclear how to uniquely distinguish "opaque" from "transparent" sources.

2.4   Non-Gaussian Features of the Correlator and q-Moments

The (K-dependent) HBT radii provide a full characterization of the two-particle correlation function only if it is a Gaussian in q or, equivalently, if the effective source $S(x, K)$ is a Gaussian in x. However, in many physical situations the source is not characterized by just one, but by several distinct length scales. In this case the Gaussian approximation of section 2.2 breaks down.

2.4.1   Resonance decays

The most important physical processes leading to a non-Gaussian shape of the correlator are resonance decays [62, 73–77, 18]. Especially longlived resonances which decay into pions cause a long-range exponential tail in the pion emission function which distorts the two-particle correlation function at small relative momentum q (see example in Figure 4 below). According to [77,78] the resonances can be classified into three classes:

1. *Short-lived resonances* ($\Gamma > 30$ MeV) which (especially if heavy) decay very close to their production point. Their most important effect is to add a contribution proportional to their lifetime to the emission duration [74, 77], thereby affecting R_l^2 and R_o^2 in the Cartesian and R_0^2 in the

YKP parametrization, but not the transverse radius $R_\perp$. They do not spoil the Gaussian parametrization.

2. *Long-lived resonances* ($\Gamma \ll 1$ MeV), mostly the η, η', K_S^0 and hyperons. These resonances travel far outside the original source before decaying. The resulting wide tail in the emission function contributes to the correlator only at very small relative momenta. This region is experimentally inaccessible due to finite two-track and momentum resolution, and the contribution from this "halo" [76] to the correlator is thus missed in the experiment. The result is an apparent decrease of the correlation strength (*i.e.* the intercept λ). In the measurable q-range the *shape* of the correlator is not affected.

3. *The ω meson* ($\Gamma = 8.4$ MeV) is not sufficiently longlived to escape detection in the correlator. Its lifetime is, however, long enough to create a measurable exponential tail in the pion emission function which distorts the shape of the correlator, giving it extra weight at small q and destroying its Gaussian form.

In practice the pions from short-lived resonances can thus be simply added to the directly emitted ones into an emission function for the "core" [73, 76]. The "halo" from long-lived resonances is accounted for by a reduced intercept parameter

$$\lambda(\boldsymbol{K}) = \left(1 - \sum_r f_r(\boldsymbol{K})\right)^2,\tag{52}$$

where the sum goes over all longlived resonances and $f_r(\boldsymbol{K})$ is the fraction of pions with momentum $\boldsymbol{K}$ stemming from resonance r. A correspondingly modified Cartesian parametrization for the correlator reads

$$C(\boldsymbol{q}, \boldsymbol{K}) = 1 \pm \lambda(\boldsymbol{K}) \exp\left(-\sum_{ij} R_{ij}^2(\boldsymbol{K}) q_i q_j\right).\tag{53}$$

Pions from ω decays must, however, be considered explicitly and, if sufficiently abundant, the resulting correlator is no longer well described by the ansatz (53).

In heavy-ion collisions the resonance fractions f_r are unknown since most resonances cannot be reconstructed in the high-multiplicity environment. Thus $\lambda(\boldsymbol{K})$ in (53) is an additional fit parameter. Its value is very sensitive to non-Gaussian distortions in the correlator, and so are the HBT radii extracted from a fit to the function (53). In theoretical studies [77] it was found that differences of more than 1 fm in the fitted HBT radii can occur if the fit is performed with λ fixed to its theoretical value (52) or if, as done in experiment, λ is fitted together with the radii. In the latter case resonance contributions (including the ω) affect the fitted radii much less than in the former. This difference in procedure may largely explain the consistently larger resonance contributions to the HBT radii found by Schlei et al. [73, 75], compared to the much weaker effects reported in [77]. Whereas Schlei et al. [73, 75] find that resonances, whose decay pions contribute only to the region of small $K_\perp$, add considerably to the $M_\perp$-dependence of $R_s = R_\perp$ and thus contaminate the transverse flow signature, practically no such effect was found in [77].

2.4.2 q-moments

In view of these systematic uncertainties one may ask for a more quantitative characterization of correlation functions whose shape deviates from a Gaussian. This can be achieved via the so-called q-moments of the correlator [77]. In this approach the matrix of Cartesian HBT parameters $\mathcal{R} \equiv (R_{ij}^2(\boldsymbol{K}))$ $(i,j = o,s,l)$ and the correlation strength $\lambda(\boldsymbol{K})$ are calculated from the following integrals:

$$\frac{1}{2}\left(\mathcal{R}^{-1}\right)_{ij} = \langle\!\langle q_i\, q_j \rangle\!\rangle(\boldsymbol{K}) = \frac{\int d^3q\; q_i\, q_j\, [C(\boldsymbol{q},\boldsymbol{K}) - 1]}{\int d^3q\, [C(\boldsymbol{q},\boldsymbol{K}) - 1]}, \tag{54}$$

$$\lambda(\boldsymbol{K}) = \sqrt{\det \mathcal{R}(\boldsymbol{K})/\pi^3} \int d^3q\, [C(\boldsymbol{q},\boldsymbol{K}) - 1]. \tag{55}$$

Similar expressions exist for the YKP parameters [77]. For a Gaussian correlator this gives the same HBT parameters as a Gaussian fit; for non-Gaussian correlators the HBT radius parameters and intercept are *defined* by (54,55).

Deviations of the correlator from a Gaussian shape are then quantified by higher order q-moments. Formally they can be obtained as derivatives at the origin of the relative source function $S_{\boldsymbol{K}}(\boldsymbol{r})$ which acts as generating function [77]:

$$\langle\!\langle q_{i_1} \cdots q_{i_n} \rangle\!\rangle(\boldsymbol{K}) = \frac{(-i\partial)^n}{\partial r_{i_1} \cdots \partial r_{i_n}} \ln S_{\boldsymbol{K}}(\boldsymbol{r})\Big|_{\boldsymbol{r}=0}. \tag{56}$$

Practical applications of this method are limited by severe statistical requirements for the measured correlator. So far they have been restricted to uni-directional moments along one of the three q-axes. The leading deviation of $C(\boldsymbol{q},\boldsymbol{K})$ from a Gaussian shape is then given by the *kurtosis* [77]

$$\Delta_i(\boldsymbol{K}) = \frac{\langle\!\langle q_i^4 \rangle\!\rangle}{3\langle\!\langle q_i^2 \rangle\!\rangle^2}(\boldsymbol{K}) - 1\,, \quad i = o,s,l. \tag{57}$$

In [77] the influence of transverse flow and resonance decays on the transverse HBT radius $R_s = R_\perp$ on the kurtosis $\Delta_s(K_\perp)$ was studied for sources of the type (41). It was found that decay pions give a positive contribution to the kurtosis which disappears at large $K_\perp$ together with the resonance fractions $f_r(\boldsymbol{K})$. Transverse flow, on the other hand, leads to a vanishing or very small negative kurtosis which tends to become larger with $K_\perp$. The sign and $K_\perp$-dependence of the kurtosis thus provide a possibility to check whether a measured $K_\perp$-dependence of R_s is really due to transverse flow or "faked" by resonance decays [77].

2.5   *The Average Freeze-out Phase-Space Density*

Bertsch [79] pointed out that by combining measurements of single-particle momentum spectra and two-particle correlations one can determine the spatially averaged phase-space density at freeze-out and thereby test local thermal equilibrium in the pion source created in high energy nuclear collisions:

$$\langle f \rangle(p) = \frac{\int_\Sigma f^2(x,p)\, p^\mu d^3\sigma_\mu(x)}{\int_\Sigma f(x,p)\, p^\mu d^3\sigma_\mu(x)}. \tag{58}$$

Here $d^3\sigma(x)$ is the normal vector on a space-like space-time hypersurface $\Sigma(x)$. According to Liouville's theorem, Σ is arbitrary as long as its time arguments are later than the time $t_{\mathrm{f}}(\boldsymbol{x})$ at which the last pion passing the surface at point $\boldsymbol{x}$

was produced. If the measured single-particle $p_\perp$-spectrum is parametrized by an exponential with inverse slope parameter $T_{\text{eff}}(y)$ and the two-particle correlation function by the Gaussian (27), one finds [23, 79, 22]

$$\langle f \rangle(K_\perp, Y) = \frac{\sqrt{\lambda(K_\perp, Y)}\, (dn/dY)\, (2\pi T_{\text{eff}}^2(Y))^{-1}\, e^{-K_\perp/T_{\text{eff}}(Y)}}{\pi^{-3/2}\, E_p\, R_s(K_\perp, Y)\sqrt{R_o^2(K_\perp, Y) R_l^2(K_\perp, Y) - R_{ol}^4(K_\perp, Y)}} \, . \quad (59)$$

The numerator (where dn/dY denotes the multiplicity density of a *single* charge state) gives the momentum-space density at freeze-out while the denominator reflects the space-time structure of the source and can be interpreted as its covariant homogeneity volume for particles of momentum $\boldsymbol{K}$. The factor $\sqrt{\lambda}$ ensures [23] that only the contributions of pions from the decays of short-lived resonances, which happen close to the primary production points, are included in the average phase-space density (see section 2.4.1).

2.6   *The Usefulness of 3-Particle Correlations*

Two-particle correlations are insensitive to the phase of the two-particle exchange amplitude: writing the latter for two particles with momenta $p_{i,j}$ as

$$\int d^4x\, S\left(x, \tfrac{1}{2}(p_i + p_j)\right)\, e^{i(p_i - p_j)\cdot x} = \rho_{ij}\, e^{i\phi_{ij}} \,, \quad (60)$$

the phase ϕ_{ij} is seen to drop out from the correlator (12). This is no longer true for higher-order multiparticle correlations. For example, for a *completely chaotic* source the true 3-particle correlator, with all two-particle correlation contributions $R_2(i,j) = C(\boldsymbol{p}_i, \boldsymbol{p}_j) - 1$ removed,

$$R_3(\boldsymbol{p}_1, \boldsymbol{p}_2, \boldsymbol{p}_3) = C_3(\boldsymbol{p}_1, \boldsymbol{p}_2, \boldsymbol{p}_3) - R_2(1,2) - R_2(2,3) - R_2(3,1) - 1, \quad (61)$$

and properly normalized,

$$r_3(\boldsymbol{p}_1, \boldsymbol{p}_2, \boldsymbol{p}_3) = \frac{R_3(\boldsymbol{p}_1, \boldsymbol{p}_2, \boldsymbol{p}_3)}{\sqrt{R_2(1,2)\, R_2(2,3)\, R_2(3,1)}}, \quad (62)$$

gives the sum of phases of the three two-particle exchange amplitudes [80]:

$$r_3(\boldsymbol{p}_1, \boldsymbol{p}_2, \boldsymbol{p}_3) = 2\cos\left(\phi_{12} + \phi_{23} + \phi_{31}\right) \equiv 2\cos\Phi \,. \quad (63)$$

Expanding the two-particle exchange amplitude (60) for small relative momenta one finds [80]

$$\begin{aligned}
\Phi \;=\; & \tfrac{1}{2} q_{12}^\mu q_{23}^\nu \left[\frac{\partial \langle x_\mu \rangle_3}{\partial \bar{K}^\nu} - \frac{\partial \langle x_\nu \rangle_3}{\partial \bar{K}^\mu} \right] \\
& -\frac{1}{24} [q_{12}^\mu q_{12}^\nu q_{23}^\lambda + q_{23}^\mu q_{23}^\nu q_{12}^\lambda] \left[\frac{\partial^2 \langle x_\mu \rangle_3}{\partial \bar{K}^\nu \partial \bar{K}^\lambda} + \frac{\partial^2 \langle x_\nu \rangle_3}{\partial \bar{K}^\lambda \partial \bar{K}^\mu} + \frac{\partial^2 \langle x_\lambda \rangle_3}{\partial \bar{K}^\mu \partial \bar{K}^\nu} \right] \\
& -\frac{1}{2} q_{12}^\mu q_{23}^\nu\, (q_{12} + q_{23})^\lambda\, \langle \tilde{x}_\mu \tilde{x}_\nu \tilde{x}_\lambda \rangle_3 + O(q^4) \,.
\end{aligned} \quad (64)$$

Here $q_{ij} = p_i - p_j$ (with $q_{12} + q_{23} + q_{31} = 0$) are the two-particle relative momenta and $\bar{K} = (p_1 + p_2 + p_3)/3$ is the average momentum of the particle triplet; the averages $\langle \ldots \rangle_3$ are calculated with the emission function $S(x, \bar{K})$. Eq. (64) shows

that Φ depends on the odd space-time variances $\langle \tilde{x}^3 \rangle$ etc. of the emission function and on the derivatives with respect to $\bar{K}$ of the point of highest emissivity $\langle x \rangle_3$. These reflect the asymmetries of the source around its center. In the Gaussian approximation of section 2.2.1 they vanish.

These considerations show that the true three-particle correlator contains additional information which is not accessible via two-particle correlations. In practice, however, it is difficult to extract this information. The leading contribution to Φ is of second order in the relative momenta q_{ij}, and in many reasonable models it even vanishes [81]. Therefore new information typically enters $r_3(\boldsymbol{p}_1, \boldsymbol{p}_2, \boldsymbol{p}_3)$ at sixth order in q. The measurement of the phase Φ is thus very sensitive to an accurate removal of all leading q^2-dependences by a proper determination and normalization of the two-particle correlator.

On the other hand, it was pointed out that the intercept of the normalized true three-particle correlation parameter r_3 may provide a good test for the chaoticity of the source. Writing the emission function for a *partially coherent* source as $S = S_{\text{cha}} + S_{\text{coh}}$ and denoting the chaotic fraction of the single-particle spectrum at momentum $\boldsymbol{p}$ as $\epsilon(\boldsymbol{p})$, the intercept of r_3 is given by [80, 82]

$$\lambda_3(\bar{\boldsymbol{K}}) \equiv r_3(\bar{\boldsymbol{K}}, \bar{\boldsymbol{K}}, \bar{\boldsymbol{K}}) = 2\sqrt{\epsilon(\bar{\boldsymbol{K}})} \frac{3 - 2\epsilon(\bar{\boldsymbol{K}})}{(2 - \epsilon(\bar{\boldsymbol{K}}))^{3/2}}. \tag{65}$$

This relation is useful since, contrary to the two-particle correlation strength λ, the intercept (65) of the normalized three-particle correlator is not affected by decay contributions from long-lived resonances which cancel in the ratio (62) [80].

Complete small-q expansions of R_2 and R_3 which generalize the Gaussian parametrization (24) to the case of partially coherent sources and to three-particle correlations, improving on earlier results in [82, 83], can be found in [80]. Within a multidimensional analysis of 2- and 3-pion correlations they allow separate determination of the sizes of the homogeneity regions of the chaotic and coherent source components as well as the distance between their centers.

3   TWO-PARTICLE CORRELATIONS FROM DYNAMICAL MODELS

Interpretation of correlation functions measured in heavy-ion collisions requires understanding the true relationship of the parameters extracted from fitting the data and the actual single-particle distributions at freeze-out. The level to which this works in practice can be established by using an event generator to model the collision dynamics, particle production and hadronic rescattering, and then constructing a two-particle correlation function. These functions can be fit in the same way as experimental correlation functions and the fit parameters compared to the single-particle freeze-out distribution in the event generator [78, 84].

The event generator correlation functions are constructed from the positions and momenta representing the single particle emission distribution at the time of the last strong interaction (*i.e.* at freeze-out). The subsequent calculation of correlation functions uses particle pairs drawn randomly from this list and constructs a two-particle symmetrized wave function [85, 55, 78, 22]. Coulomb wave functions for the particles are used. As for experimental data, a Coulomb correction is applied to the correlation function before fitting [78].

As the event generator yields a correlation function while simultaneously knowing the space-time distribution and history of the same particles, discrepancies

between the fit parameters and freeze-out distributions may be resolved. Furthermore, the generated particles may be subjected to experimental acceptance cuts and treated like real data. This allows evaluation of the effects of experimental acceptances and analysis techniques. Since a significant number of the observed hadrons arise from decay of long-lived resonances, the event generators can also quantify their effects on the correlation functions. Such studies were performed using the RQMD [86, 78, 87–89] and ARC event generators [90, 84] as well as hydrodynamical simulations [73, 91, 75, 92–94].

3.1   RQMD

Many experiments use the RQMD event generator [86], as it satisfactorily reproduces single-particle distributions. RQMD simulates the microscopic phase-space evolution, using resonance and string excitation as primary processes, followed by fragmentation, decays and subsequent hadronic collisions. Many features in p-nucleus and nucleus-nucleus collisions which can be related to secondary scattering are well described by RQMD [95, 96]. The numerous secondary collisions result in considerable transverse flow of RQMD events before freeze-out [78,97,56].

3.1.1   Collective expansion

Figure 4 shows a comparison of RQMD freezeout positions and correlation functions for S+Pb collisions at 200 GeV/nucleon [78]. The top half shows the pion (solid lines) and kaon (dotted lines) position distributions at freeze-out along and
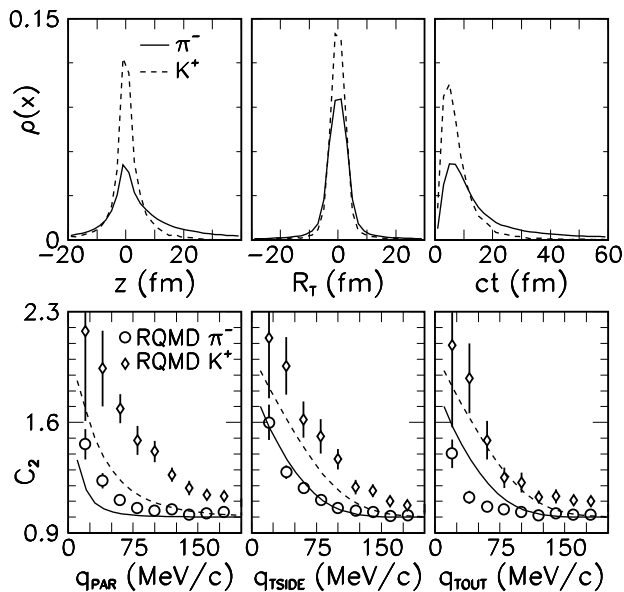

Figure 4: Comparison of position distributions at freeze-out and calculated correlation functions, both from RQMD events. The lines in the bottom figures show $1 + |\tilde{\rho}(q)|^2$ where $\tilde{\rho}(q)$ is the Fourier transform of the corresponding distribution in the upper figures. The notation on the axes $q_{\text{PAR}}, q_{\text{TSIDE}}, q_{\text{TOUT}}$ corresponds to q_l, q_s, q_o used elsewhere in this review. (Figure taken from [78].)

transverse to the beam direction as well as in time, integrated over their momenta.

The kaon distributions are narrower than those of the pions. The lower section of the figure shows correlation functions calculated from the RQMD events, plotted as functions of the Cartesian variables. The points show the calculated correlation functions using the NA35 experimental acceptance, while the solid and dashed lines indicate Fourier transforms of the relevant components of the pion and kaon freeze-out distributions in the top row of figures. If the particle positions and momenta were uncorrelated, HBT interferometry should reproduce the full size of the freeze-out distribution, and in the lower panels the lines should agree with the corresponding points. Instead, the correlation functions calculated from the RQMD *phase-space* distribution are much wider in q_l than expected from the Fourier transform, indicating a smaller effective source. This reflects longitudinal position-momentum correlations arising from a strong longitudinal expansion of the source. As will be seen later, this prediction by RQMD and hydrodynamical models is confirmed by the data. An analogous effect is seen in the sideward direction where especially the calculated kaon correlation function is wider than expected from the Fourier transform of their momentum-integrated transverse spatial distribution. This can be traced back to transverse position-momentum correlations in the RQMD freeze-out distribution, induced by collective transverse expansion. As discussed above, these correlations increase with increasing transverse mass of the particles and are thus more strongly reflected in the kaon correlation function. The resulting decrease of the transverse effective source size extracted from kaon correlations is again confirmed by the data.

Event generators like RQMD can be used to study the influence of experimental acceptance cuts on the $K_\perp$-dependence of the HBT fit parameters induced by collective flow. RQMD was shown to reproduce the $K_\perp$-dependence of the correlation functions both at SPS [87–89] and AGS [98,99] energies. It is noteworthy that by analyzing the *same* set of RQMD events with the NA35 and NA44 acceptances, good agreement with both data sets was obtained even though the $K_\perp$-dependence of R_s appears to be somewhat stronger in NA44 [56].

The shrinking of the effective source size as a result of collective flow is illustrated in Figure 5. The collective flow velocity has the effect of "focussing" particles arising from nearby regions of the source. As the correlation selects particles of small momentum difference, it is sensitive to this focussing. Figure 5 shows the freeze-out distributions of all pions (open histograms) and of those pions accepted in two NA44 spectrometer settings (44mr is the low $K_\perp$ setting and 131mr high $K_\perp$). Higher $K_\perp$ pairs have a narrower distribution at freeze-out due to the larger effect of the flow velocity. Note that this is the focussing from flow and not an experimental acceptance effect. The correlation function only "sees" particles which are flowing in the same direction; particles from the far side of the source flow away in an expanding source. This is why the characteristic drop of apparent source size with increasing $K_\perp$ is observed by both NA35 and NA44 even though one experiment has large acceptance and one narrow.

3.1.2 Emission duration

The emission duration is usually calculated from the fit parameters via Eq. (29), using the leading term only. Comparison of this emission time estimate with the actual width of the freeze-out time distribution from RQMD events determines the validity of neglecting the position-momentum correlation effects on the space-time variances. Fields et al. [56] found that only for $K_\perp$ below ≈ 100 MeV/c
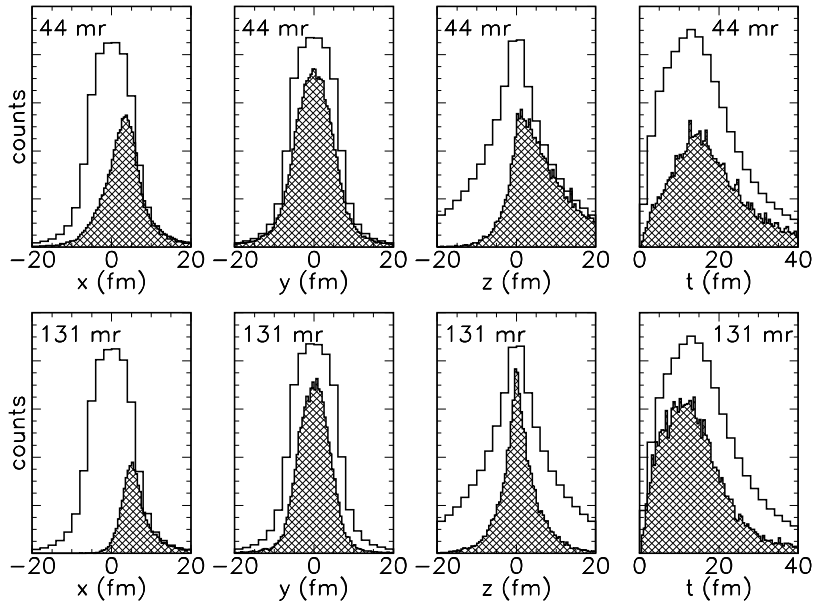
Figure 5: RQMD freeze-out distributions for pions. The open histograms give all pions from RQMD, the hatched ones only those accepted by NA44 at various spectrometer settings. x, y, z indicate the out-, side- and longitudinal directions in the collision center of mass system. (Figure taken from [89].)

does this method yield the actual emission duration. For higher $K_\perp$ particles, the true emission duration (3-6 fm/c for S+Pb [56] and 7-8.5 fm/c for Pb+Pb [89]) is shorter due to flow-induced position-momentum correlations, but the value derived from the difference between R_o^2 and R_s^2 underrepresents even this. Consequently, extraction of the emission duration from experimental correlation functions should only be attempted at low $K_\perp$.

Of course, the total lifetime of the source between impact and freeze-out is considerably larger.

3.1.3   Resonance decays

In RQMD as many as half of the low $K_\perp$ pions in heavy-ion collisions arise from the decay of long-lived resonances [78]. Very long-lived resonances produce a long tail in the pion freeze-out position distribution, visible in Figure 4. This corresponds to a component of the correlation function too narrow to measure and reduces the correlation strength λ [78]. In S+Pb collisions the fraction of pions from ω, η, η' resonances is 30% at low $p_\perp$ and falls to 5 % at $p_\perp =$ 800 MeV/c [56]. These pions cause a departure from a Gaussian source shape, which impacts the quality of fits with a Gaussian parametrization.

Resonance decay contributions to kaons are smaller, which makes the interpretation of their correlation functions cleaner. Due to their rest mass they always have a sizeable $M_\perp$, and so their correlation functions are more sensitive to flow.

3.2   Hydrodynamical Models

A more macroscopic approach to describe the dynamical evolution of the reaction zone treats it as a locally thermalized ideal fluid and solves the relativistic hydrodynamical equations. Initial conditions are usually set after an initial pre-equilibrium stage and suitably parametrized [73, 75, 91, 100]. Freeze-out is usually enforced at a fixed energy density or temperature. After the end of the simulation those fluid cells which satisfy this freeze-out criterium are identified, and the local energy and baryon density in these cells are converted into temperature and chemical potentials using the equation of state of an ideal resonance gas in thermal and chemical equilibrium. Each such cell thus emits a thermal hadron spectrum boosted by the local fluid velocity. This determines the emission function $S(x, p)$ of the model from which spectra and correlation functions can be calculated [73, 75, 92, 93].

Measured spectra and correlation functions put constraints on the output of such simulations which can be used to identify allowed combinations of initial conditions and equations of state [100, 94]. In this way certain classes of evolution scenarios can be eliminated while successful combinations can be used to predict other observables for further discrimination or hadronic one- and two-particle spectra at future colliders [101].

4   TWO-PARTICLE CORRELATIONS IN HEAVY-ION EXPERIMENTS

4.1   General Remarks and Short Overview of the Experiments

4.1.1   Construction of the correlation function

Experimentally, correlation functions are constructed by counting events with boson pairs of given pair and relative momenta and dividing by a properly normalized [6, 102] "background" sample with no enhancement:

$$C_2^{\text{expmt.}}(\boldsymbol{q}, \boldsymbol{K}) = A(\boldsymbol{q}, \boldsymbol{K})/B(\boldsymbol{q}, \boldsymbol{K}). \qquad (66)$$

Typically, $B(\boldsymbol{q}, \boldsymbol{K})$ is generated by creating artificial pairs by combining single tracks from different events, or by using unlike-sign pions. Generally, analyses bin both the data and the background in the chosen variables. The correlation functions are then corrected for Coulomb interactions, experimental resolution and two-particle acceptance (generally by Monte Carlo techniques), residual two-particle effects on the single-particle spectrum constructed from mixed pairs, particle misidentification (if contamination is significant); see [106, 103–105] for details.

4.1.2   Fit procedures

Correlation functions are customarily fit by a Gaussian in q which assumes a Gaussian-distributed source. This is a simplification, since the source may well have a more complex shape. However, the Gaussian assumption provides a reasonable representation of the data [103, 107] and continues to be used. One should keep in mind, however, that the measured correlation functions are usually not perfect Gaussians and that this leads to systematic uncertainties of the order of 10-20% in the extracted fit parameters.

High statistics data samples are now analyzed using multi-dimensional fits [13, 36, 37, 41, 57]. Unlike many lower-dimensional parametrizations these do not require the unrealistic assumption of a spherical source and are more sensitive to the collision dynamics [84]. Some analyses do, however, use lower-dimensional parameterizations due to statistical or acceptance limitations. These carry the danger of producing misleading results, but they can be useful if they are based on a complete parametrization and make proper projections [98].

4.1.3 Coulomb corrections in experiment

Initially, experimental correlation functions were corrected for 2-body Coulomb interactions using the Gamov factor. However, as measurements of heavier systems were made, the point source approximation became increasingly inappropriate. Several different techniques have been used for improved corrections.

The first experimental improvement was achieved by integrating expression (18) with Coulomb wave functions using a technique developed by Pratt [108]. For the relative source function $S_{\boldsymbol{K}}(\boldsymbol{r})$ one usually takes a spherically symmetric Gaussian in the pair rest frame with a size parameter which is iterated. In S+Pb collisions, NA44 found that the improved Coulomb correction resulted in a 5-10% increase in the fitted radius parameters for pions and kaons [103, 104, 88]. In Pb+Pb collisions, the difference is 8-12%, with λ decreasing by 3-6% [89].

The Coulomb correction can be investigated experimentally by measuring correlation functions of oppositely charged particle pairs, where quantum mechanical symmetrization effects are absent [109]. The measured Coulomb attraction reflects the (non-zero) source size [27], and can be used to parametrize a Coulomb correction for same sign pairs. This technique is used by NA49 [107].

4.1.4 Short description of the experiments

We now briefly describe the experiments whose data will be discussed in the following. E802/859/866 at the AGS is a wide acceptance magnetic spectrometer experiment, tracking particles with drift chambers and identifying them via time-of-flight. E814/877 at the AGS is a multipurpose experiment which includes a hadron spectrometer covering forward angles. Particle identification is achieved using time-of-flight with a very long flight path. The angular range of the acceptance limits the identified hadrons to rather small $p_\perp$. E895 is a time projection chamber (TPC) at the AGS, which identifies hadrons through their energy loss in the gas-filled detector volume.

At the CERN SPS, NA44 is a second generation experiment which measures single and two-particle distributions at midrapidity. It is characterized by excellent particle identification, with contaminations at the 1% level. As a focussing spectrometer, its acceptance for particle pairs with small momentum difference is optimized, allowing for high statistics in the region of the Bose-Einstein correlation signal. NA35 is a streamer chamber and TPC experiment at CERN, with a large acceptance for pions from 200 A GeV S-nucleus collisions. NA49, the successor to NA35, uses four TPC's and two time-of-flight walls to track and identify particles in Pb+Pb collisions. For the correlation functions NA35 and NA49 use charged tracks without particle identification; they are fit as a function of pair rapidity and transverse momentum.

Different experiments analyze correlations in different reference frames. The

NA44 Collaboration [104, 88] use the LCMS in which the longitudinal pair momentum vanishes. This frame couples the lifetime information solely to q_o and ensures that the source velocity in the analysis frame is usually small [57]. The NA35/NA49 Collaboration [105, 87] and E802/E859/E866 [106, 110, 111] analyze in the nucleon-nucleon center of mass frame which is similar (but for asymmetric collision systems not identical) to the LCMS at mid-rapidity.

4.1.5   Square roots of 2, 3, and 5

Confusion can easily arise when comparing fitted HBT radius parameters with the rms or hard sphere radii of the colliding nuclei. As is well known, the 3-dimensional rms radius $R_{\mathrm{rms,3d}}$ and the hard sphere radius $R_{\mathrm{box}} = 1.2\,A^{1/3}$ fm are related by a factor $\sqrt{3/5}$:

$$R_{\mathrm{rms,3d}}^2 = \langle \boldsymbol{r}^2 \rangle = \langle x_o^2 + x_s^2 + x_l^2 \rangle = \frac{\int_0^{R_{\mathrm{box}}} r^2 \, d^3 r}{\int_0^{R_{\mathrm{box}}} d^3 r} = \frac{3}{5} R_{\mathrm{box}}^2. \tag{67}$$

The HBT radii are *1-dimensional rms radii* (e.g. $R_s^2 = \langle x_s^2 \rangle$) and thus another factor $\sqrt{3}$ smaller than $R_{\mathrm{rms,3d}}$. If a cold spherical nucleus in its ground state could be induced to emit pion pairs, one would thus measure

$$R_s^{\mathrm{cold}} = \frac{R_{\mathrm{rms,3d}}}{\sqrt{3}} = \frac{R_{\mathrm{box}}}{\sqrt{5}}. \tag{68}$$

We will call the ratio of the actually measured R_s to this naive expectation the "expansion factor" ξ.

At high energies it is often useful to compare with the 2-dimensional rms radius of the nuclear overlap region in the transverse plane, $R_{\mathrm{rms,2d}} = \langle x_o^2 + x_s^2 \rangle^{1/2}$, which is a factor $\sqrt{2}$ larger than the corresponding sideward radius $R_s = R_\perp$.

4.2   A Measured Correlation Function

Collision systems with light projectiles (S+S and S+Pb at the SPS and Si+Au at the AGS) have been studied by several experiments, with some systematic differences in the results. NA35 included a factor of $\frac{1}{2}$ in the exponent of the Gaussian fit function, which yields R parameters larger by $\sqrt{2}$ than those from other experiments.

Figure 6 shows three-dimensional correlation functions of π^+ and K^+ pairs in 14.6 A GeV Si+Au collisions, measured by E859 [111]. Shown are the projections in the three Cartesian directions, with narrow cuts on the momentum differences in the other two directions. However, the fits are performed in three dimensions, not upon the projections. The solid line shows a Gaussian fit in the CM system (Y=1.25) according to (53) without the cross-terms; the shape of the data is reproduced quite well.

The fit parameters extracted by E859 from pion and kaon correlations are shown in Table 1. The radius parameters from kaons are considerably smaller than those from pions, but the λ parameter is larger [106, 110]. Both trends are expected from the fact that kaons are less affected by resonance decays than pions [112]; from the discussion in Sec. 2.4.1, however, the effect on the radius parameters should have been weaker. It was also postulated that, due to their smaller cross section with nucleons, kaons may freeze out earlier than pions [113],
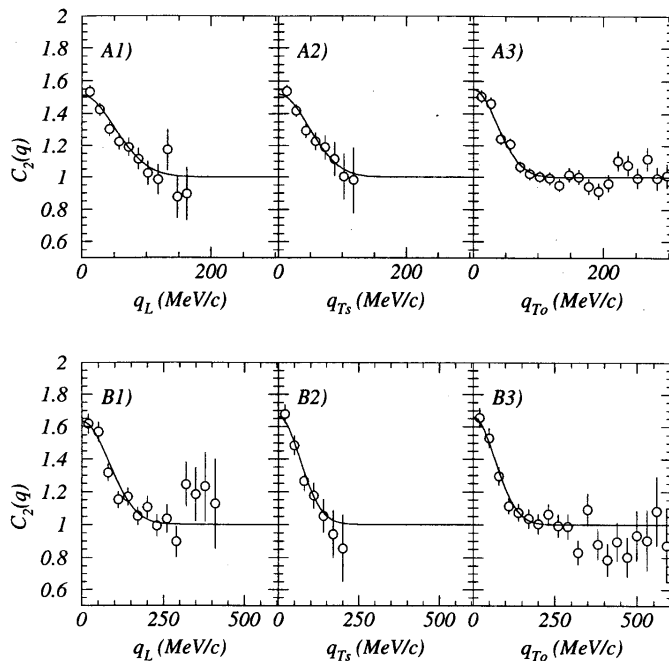
Figure 6: $\pi^+\pi^+$ and K^+K^+ correlation functions for 14.6 A GeV Si+Au collisions from E859 [111]. The analysis was done in the participant center of mass (Y=1.25). For the projections the remaining two components of the relative momentum were cut to 5 MeV/$c < q_{\mathrm{perp}} < 35$ (65) MeV/c for pions (kaons). The solid lines show a 3-d Gaussian fit. (Figure taken with permission from [111].)

reflecting a smaller source if the latter expands. The E859 analysis [111] showed, however, within a fit of reduced dimensionality (2 instead of 3 radius parameters) that also the pion correlation radii decrease systematically with increasing transverse mass of the pair. However, the interpretation of such a 2-dimensional fit is not straightforward.

4.3   Asymmetric Collision Systems: First Signs of $M_\perp$-Dependence

The first 3-dimensional and $\boldsymbol{K}$-dependent correlation analysis was achieved in sulphur-induced collisions at the SPS. Table 2 summarizes the R parameters extracted by NA44 from a 3-dimensional analysis of pion and kaon correlations in 450 GeV p+Pb and 200 A GeV S+Pb collisions at the SPS [114, 104]. They were extracted from a fit to

$$C(\boldsymbol{q}, \boldsymbol{K}) = 1 + \lambda(\boldsymbol{K})\exp(-R_s^2(\boldsymbol{K})q_s^2 - R_o^2(\boldsymbol{K})q_o^2 - R_l^2(\boldsymbol{K})q_l^2). \qquad (69)$$

One sees the same trends as observed by E802/859 at lower beam energy [110, 111]: the R parameters for kaons are consistently smaller than for pions and the correlation strength λ is larger. That the R parameters are larger in S+Pb than in p+Pb collisions should be expected. However, R_s in S+Pb collisions is also (much) larger than the projectile, even for kaons: for ^{32}S we should compare R_s to $R_{\mathrm{box}}/\sqrt{5} = 3.8\,\mathrm{fm}/2.23 = 1.7$ fm. Thus the system must have expanded significantly before freezeout.

This is supported by the additional observation (see Figure 7) that all three R

pair	R_l	R_s	R_o	λ
$\pi^+\pi^+$	2.75±0.15	2.95±0.19	3.77±0.13	0.65±0.02
K^+K^+	1.71±0.14	2.09±0.20	2.07±0.16	0.83±0.08

Table 1: E859 correlation function fit parameters [111]. Pions have rapidities $1.2 < y < 1.8$ and transverse momenta 100 MeV/$c < p_\perp < 800$ MeV/c, while kaons are accepted for $1.0 < y < 1.7$ and 100 MeV/$c < p_\perp < 900$ MeV/c.

		R_s	R_o	R_l	λ
S + Pb	π^+	4.15±0.27	4.02±0.14	4.73±0.26	0.56±0.02
p + Pb	π^+	2.00±0.25	1.92±0.13	2.34±0.36	0.41±0.02
S + Pb	K^+	2.55±0.20	2.77±0.12	3.02±0.20	0.82±0.04
p + Pb	K^+	1.22±0.76	1.53±0.17	2.40±0.30	0.70±0.07

Table 2: HBT parameters in the LCMS measured by NA44 for 450 GeV p+Pb and 200 A GeV S+Pb collisions [114, 104]. Pions are measured in $3.2 < y < 4.2$, kaons in $2.7 < y < 3.3$. The $p_\perp$ acceptance is $0 < p_\perp < 0.6$ GeV/c for both.

parameters show a strong dependence on the transverse mass $M_\perp$ of the pairs. In [88] they were compared to a common $1/\sqrt{M_\perp}$-law (see Figure 7) which simultaneously reproduces the two pion points and one kaon point in each of the three Cartesian directions. This points to a dependence on $M_\perp$ (rather than on m_0 and $K_\perp$ separately), as expected for a thermalized expanding source [39].

NA44 compared correlations of K^+ and K^- pairs, to investigate possible effects of their different cross sections with nucleons on the freeze-out distribution. No significant differences were found, indicating that at SPS energies the KN cross section plays a subdominant role in the freeze-out process. This is to be expected from the small measured nucleon/pion ratio: $p/\pi^+ = 0.12$ [115]; $K\pi$ scattering dominates and is similar for K^+ and K^-.

The fit function (69) did not include the cross-term R_{ol}. It is expected to be small near mid-rapidity where the NA44 acceptance is concentrated. Subsequent analyses showed [89] that including the cross-term changes the R parameters by $\lesssim 10\%$, less than the 20% systematic uncertainty on their absolute values.

NA35 has measured the rapidity and transverse momentum dependence of the three source radius parameters R_s, R_o, and R_l for central S+S, S+Cu, S+Ag, and S+Au collisions [105], by fitting the correlation functions to Eq. (69) in the nucleon-nucleon center of mass. The rapidity dependence of the transverse radius parameters is minimal. R_l depends strongly on the pair rapidity and is well described by $R_l \sim 1/\cosh(Y - Y_{\rm CM})$, indicating approximately boost-invariant longitudinal expansion [67] as was predicted for collisions at these energies [116]. If this Y-dependence in the CM frame were exact, R_l would be independent of Y in the LCMS. One should remember, however, that the analysis of [105] was done without including the R_{ol} cross-term which was shown [47] to become sizeable in the CM at large $Y - Y_{\rm CM}$.

All systems show a similar dependence of R_l on the transverse pair momentum $K_\perp$, with R_l decreasing with increasing $K_\perp$ at a similar rate as found by NA44 (see above). This provides further evidence for longitudinal expansion of the
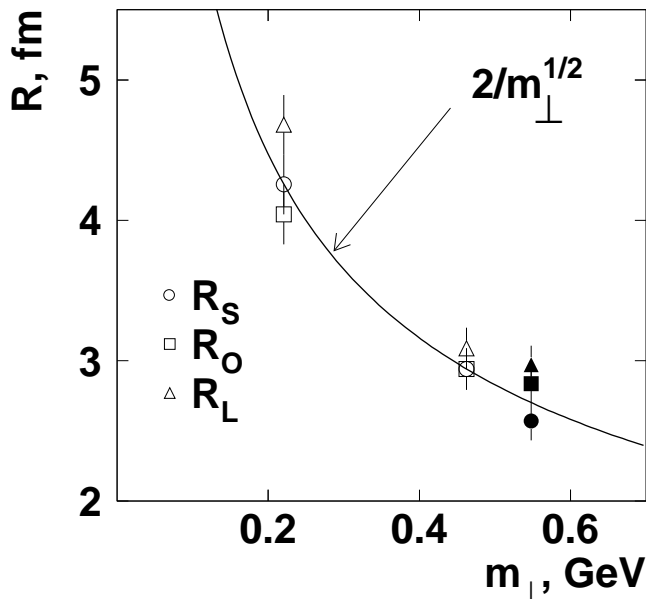
Figure 7: $M_\perp$-dependence of the three Cartesian radius parameters in 200 A GeV S+Pb collisions measured by NA44 [88]. The open (filled) symbols indicate values extracted from $\pi^+\pi^+$ (K^+K^+) correlations. The solid line is given by $R = 2$ fm$/\sqrt{M_\perp}$ ($M_\perp$ in GeV).

source (see Sec. 2.3), and this behaviour is also predicted by hydrodynamical simulations of the collisions [92, 105].

Compared to R_l, the transverse parameters R_s, R_o from the NA35 analysis [105] show a weaker $K_\perp$-dependence, indicating that the longitudal and transverse expansions differ. Such a tendency is generically expected from hydrodynamic simulations of the collision dynamics [92,93] and from the model studies presented in Sec. 2.3. As discussed in section 3.1.1, the apparently stronger $K_\perp$-dependence of the transverse R parameters observed by NA44 in S+Pb collisions [88] can be understood in terms of the different experimental acceptances.

4.4 Au+Au Collisions at the AGS

Collective transverse expansion of the emitting source was also observed at the AGS. A characteristic $K_\perp$ dependence of the transverse radius parameter $R_\perp$ was found in Au+Au collisions at 11 GeV/nucleon by E866 [98]. Decreasing values of all three Cartesian source parameters with increasing $K_\perp$ are observed in Au + Au collisions at energies as low as 2 GeV/nucleon by the E895 collaboration [99], although at their lowest beam energy of 2 Gev/nucleon the $K_\perp$ dependence of R_s and R_o seems to disappear. Though the hadron densities at such energies are much less than at 158 GeV/nucleon, they are still quite large. Even here, the hadronic scattering can generate pressure and cause the source to expand. In fact, pair momentum dependence of the fit parameters was already observed in streamer chamber data at the Bevalac by Beavis et al. [117] in a 1-dimensional analysis of pion correlations from 1.8 GeV/nucleon Ar+Pb collisions. Already at that time the dependence was interpreted as evidence for expansion of the source before freeze-out [117].

4.5   Pb+Pb Collisions at the SPS

4.5.1   Cartesian parametrization

Figure 8 shows projections of the 3-dimensional correlation functions for π^- and π^+ pairs from 158 GeV/nucleon Pb+Pb collisions, measured by NA44 (closed points) [89]. The left column shows a 1-dimensional analysis in q_{inv} for com-
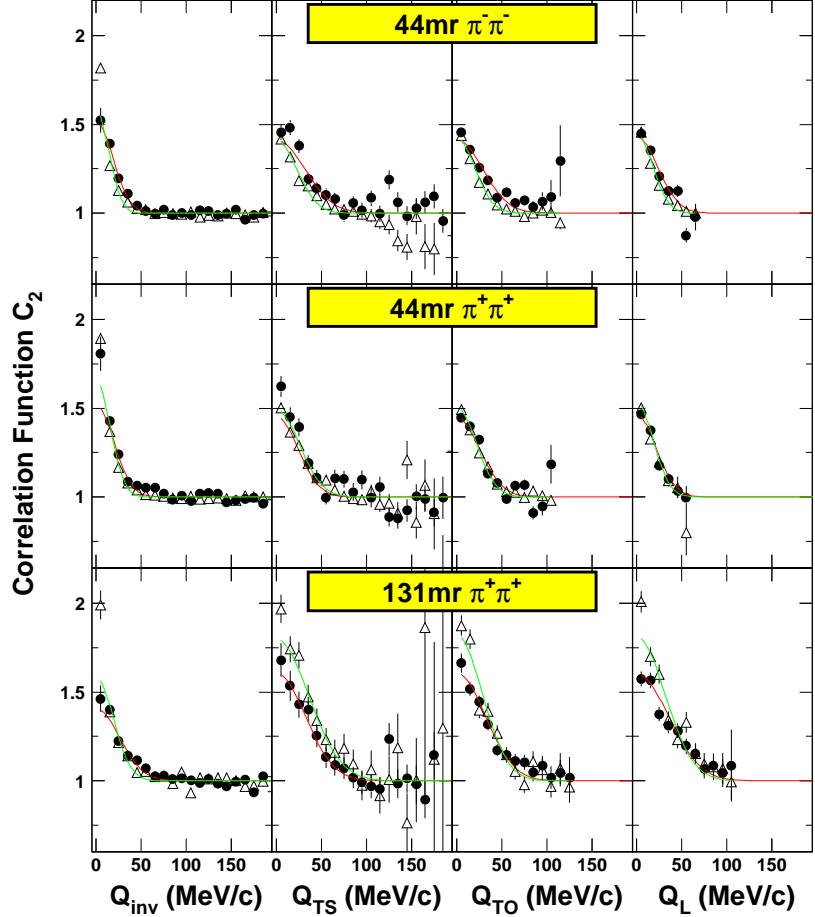

Figure 8: Comparison of NA44 Pb+Pb $\pi^+\pi^+$ correlation data (solid circles) and RQMD predictions (open triangles). The 1-dimensional projections of the 3-dimensional correlation function are averaged over the lowest 20 MeV/c in the other momentum differences. (Figure taken from [89].)

parison with older data from other colliding systems. Two angular settings of the spectrometer cover $p_\perp$-ranges of 0-0.4 GeV/c and 0.3-0.8 GeV/c. The fitted source parameters, with and without the R_{ol} cross-term, are given in Table 3 [89]. As in the case of sulphur-induced collisions, all R parameters are seen to become significantly smaller as $K_\perp$ increases, again pointing to collective longitudinal and transverse flow of the source. At small $K_\perp$ R_s is once again much larger than the corresponding value (3.1 fm) of a cold Pb nucleus, indicating that the transverse *flow* also leads to transverse *growth* of the collision zone before freeze-out.

The cross-term R_{ol}^2 is non-zero for all data sets, and it is rather large for the

pair ($\langle K_\perp \rangle$)	λ	R_o (fm)	R_s (fm)	R_l (fm)	R_{ol}^2 (fm^2)
$\pi^-\pi^-(\approx 170)$	0.495±0.023	4.88±0.21	4.45±0.32	6.03±0.35	
$\pi^+\pi^+(\approx 170)$	0.569±0.035	5.50±0.26	5.87±0.58	6.58±0.48	
$\pi^+\pi^+(\approx 480)$	0.679±0.034	4.39±0.18	4.39±0.31	3.96±0.23	
$\pi^-\pi^-(\approx 170)$	0.524±0.026	5.35±0.25	5.07±0.35	6.68±0.39	10.7±2.9
$\pi^+\pi^+(\approx 170)$	0.658±0.035	5.98±0.23	6.94±0.48	7.39±0.40	28.1±3.5
$\pi^+\pi^+(\approx 480)$	0.693±0.037	4.59±0.21	4.71±0.36	4.15±0.25	3.1±1.4

Table 3: Cartesian radius parameters from a Gaussian fit to NA44 correlation functions for Pb+Pb collisions [89] using the Coulomb wave correction. The fitted results with and without the cross-term R_{ol}^2 are shown. ($\langle K_\perp \rangle$ in MeV/c.)

low-$K_\perp$ π^+ pairs. As explained above, this term should be non-zero in the LCMS frame (where these data were analyzed) if the source is not reflection symmetric in beam direction. Since the NA44 low-$K_\perp$ acceptance is slightly forward of midrapidity, this condition of symmetry is not fulfilled. The fitted R parameters all become larger when the cross-term is included. The higher $K_\perp$ acceptance is nearer midrapidity, and the cross-term is indeed smaller.

It should be noted that the fit parameters for positively and negatively charged pions differ in an apparently significant way. However, calculation of the χ^2 per degree of freedom between the two *measured* correlation functions yields a value of 450/440 [89]. As this is near unity, the experimenters concluded that the correlation functions do not, in fact, differ. This illustrates an important systematic limitation in extracting source parameters from Gaussian fits to measured correlation functions. Such problems are certainly exacerbated when comparing data from different experiments where statistical and systematic errors depend differently on $\boldsymbol{q}$. These limitations hold regardless of the choice of source parametrization, but a comparison of different parametrizations (in which the available $\boldsymbol{q}$-space is differently populated) via the cross-check relations given in Sec. 2.2 could provide an estimate for the corresponding systematic uncertainties.

Figure 8 also shows pion correlation functions calculated from the RQMD event generator [86], using the same charged multiplicity as selected by the experiment and a filter simulating the NA44 acceptance. RQMD predicts source size parameters which are slightly larger than the measured ones [89], but agrees remarkably well with the general trend of the data. It reproduces the larger values of R_l compared to the transverse R parameters for low $K_\perp$ and predicts radius parameters similar to the measured ones at high $K_\perp$. It overpredicts, however, significantly the value of the correlation strength λ. This discrepancy is likely due to non-Gaussian distortions of the correlation function by pions from resonance decays and the resulting systematic uncertainties in Gaussian fits (see Sec. 2.4.1).

4.5.2 Yano-Koonin-Podgoretskiĭ parametrization

An analysis of charged particle correlations from 158 A GeV Pb+Pb collisions with the Yano-Koonin-Podgoretskiĭ parametrization (30) (amended by a correlation strength parameter λ) was performed by the NA49 Collaboration [118,107]. The analysis is not based on identified pions, and the non-pion contamination (which contributes to the mixed-pair background but not to the correlated pairs)

reduces the value of λ significantly. However, the values of the YKP fit parameters are affected only at the 2-6% level [107].

The left part of Figure 9 shows the fit results for the parameters $R_{\parallel}, R_{\perp}$ and R_0, both as a function of pair rapidity $Y \equiv Y_{\pi\pi}$ for small transverse pair momentum $0.1 < K_{\perp} < 0.2$ GeV/c and as a function of $K_{\perp}$ for forward moving pairs at $3.9 < Y < 4.4$. $R_{\parallel}$ and $R_{\perp}$ peak at midrapidity, the maximum of $R_{\parallel}$ ($\approx 7-8$
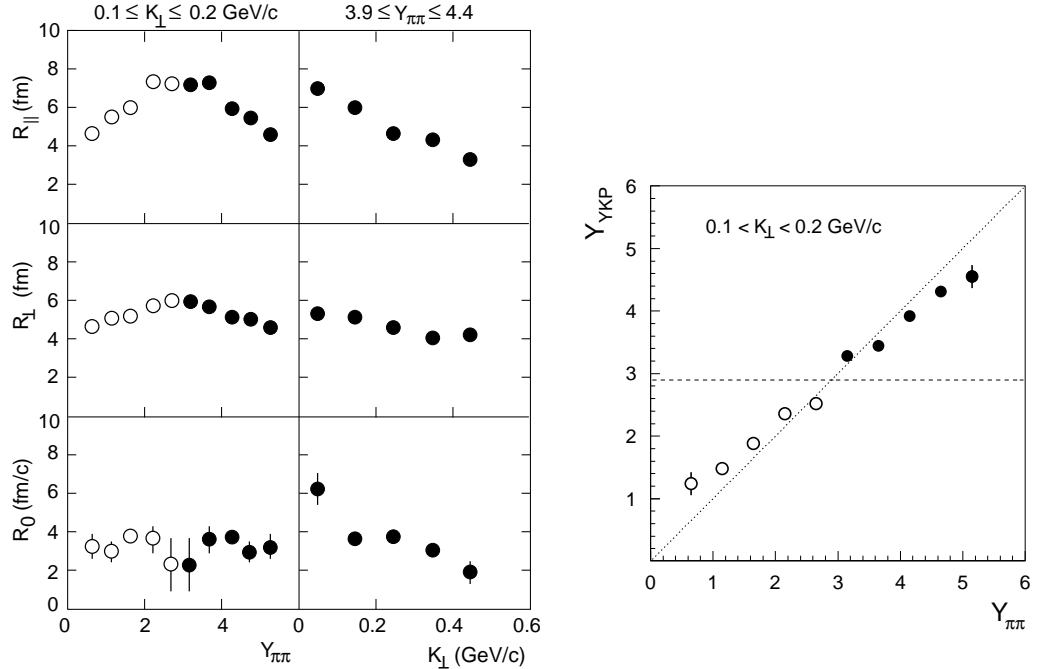

Figure 9: Left: YKP radius parameters for pion pairs from 158 A GeV Pb+Pb collisions measured by NA49, as functions of the transverse momentum $K_{\perp}$ and rapidity $Y \equiv Y_{\pi\pi}$ as indicated in the Figure. Right: Effective source rapidity Y_{YK} for pions as a function of pair rapidity $Y \equiv Y_{\pi\pi}$, for pairs with small transverse momenta ($0.1 < K_{\perp} < 0.2$ GeV). The dashed horizontal line indicates the expectation from a non-expanding source. Filled circles are measured data, open circles are reflected about midrapidity ($Y_{\pi\pi} = 2.9$). (Figure taken with permission from [107].)

fm) being somewhat larger than that of $R_{\perp}$ (≈ 6 fm, more than twice as large as expected from the initial nuclear overlap region). Since at midrapidity $R_l = R_{\parallel}$, the NA49 YKP radius parameters $R_{\parallel}, R_{\perp}$ can be compared with R_l, R_s from NA44; they are consistent. While all three YKP radius parameters are decreasing functions of $K_{\perp}$, the $K_{\perp}$-dependence of $R_{\parallel}$ is clearly stronger than that of $R_{\perp}$, indicating dominant longitudinal and somewhat weaker transverse expansion.

The right diagram in Figure 9 shows a strong correlation between the effective source rapidity Y_{YK} extracted from the YKP fit and the pair rapidity $Y_{\pi\pi}$. Following the discussion in Sec. 2.3.1 this is again evidence for very strong longitudinal expansion of the source. The data points in the Figure seem to indicate a slope slightly below unity, as expected from thermal smearing effects at low $K_{\perp}$ (see Figure 3).

The data were compared [107] to the expanding source model (41). In each Y-bin the $K_{\perp}$-dependence of the R-parameters can be successfully described by the

model, and in particular the strong $K_\perp$-dependence is reproduced very well by the assumption of *boost-invariant* longitudinal flow. The rapidity dependence of $R_\perp$, however, cannot be reproduced by a constant transverse Gaussian radius R of the source; it requires R (and thereby the average transverse flow) to decrease away from midrapidity [63, 64]. Near midrapidity one finds for the model parameter R in (41) $R \approx 8$ fm, shrinking to $R \approx 7$ fm at $3.9 < Y < 4.4$ [107]. From (47) one obtains the ratio $\eta_f^2/T = 3.7 \pm 1.6$ GeV^{-1} [107]. For freeze-out temperatures in the range 100-140 MeV this implies transverse flow rapidities η_f of 0.6-0.72, corresponding to average transverse flow velocities of 0.5-0.6c.

4.5.3   Emission duration

In sulphur-induced collisions at the SPS [105, 88] and in Pb+Pb collisions analyzed by NA44 with the Cartesian parameterization [89] the emission duration was found to be very short – consistent with 0-2 fm/c (with considerable statistical and systematic uncertainties). NA49 found from their YKP fit to the Pb+Pb data a non-zero emission duration of approximately 3 fm/c [107]. All these numbers are rather short compared to the emission duration predicted by RQMD, namely 3-6 fm/c for S+Pb [56] and 7-8.5 fm/c for Pb+Pb [89], despite the fact that RQMD provides a good representation of the particle distributions. This illustrates the difficulty and model dependence of extracting the emission duration in relativistic heavy ion collisions, discussed in the previous sections.

This is different for low-energy heavy-ion collisions at E/A=30-80 MeV where emission durations of up to 1400 fm/c were measured [119] – the typical evaporation time of a compound nucleus. Such large times can be extracted with relatively much less model uncertainty. If the creation of a quark-gluon plasma led to a very long-lived intermediate stage near the critical temperature T_c for hadronization, it could emit hadrons from the surface over much longer periods of time than presently measured. This might leave more easily interpretable traces in R_{diff}^2 or R_0^2 [43, 54, 91].

5   COMBINING SINGLE- AND TWO-PARTICLE SPECTRA

It has been shown that the single-particle $m_\perp$-distributions of pions and heavier hadrons reflect a transversely expanding source [72, 120, 65]. Such spectra are sensitive to a different combination of T and η_f [70, 72]. Combining this information with that from the two-particle correlation functions thus allows a separation of the collective and thermal momentum components described by η_f and T [121, 39, 122, 63].

NA49 has analyzed negative hadron and deuteron spectra in Pb+Pb collisions at the SPS and combined the fit parameters with their correlation function analysis near midrapidity [107]. Figure 10 shows the allowed regions of freeze-out temperature and radial velocity as bands of $\pm\sigma$ around each of the three independent fits. These favor a narrowly defined overlap region with $T = 120 \pm 12$ MeV and $\eta_f = 0.55 \pm 0.12$ [107]. From the model parameter, η_f, one can calculate the average transverse flow velocity $\langle v_\perp \rangle$ (see below), given the density and velocity profiles. The fit to the h^- spectrum in [107] was made without explicit consideration of the contributions from resonance decays and heavier hadrons; once these are included [123], the band labelled "h^-" in Figure 10 no longer bends over at small T, and the crossing region is shifted slightly downward.
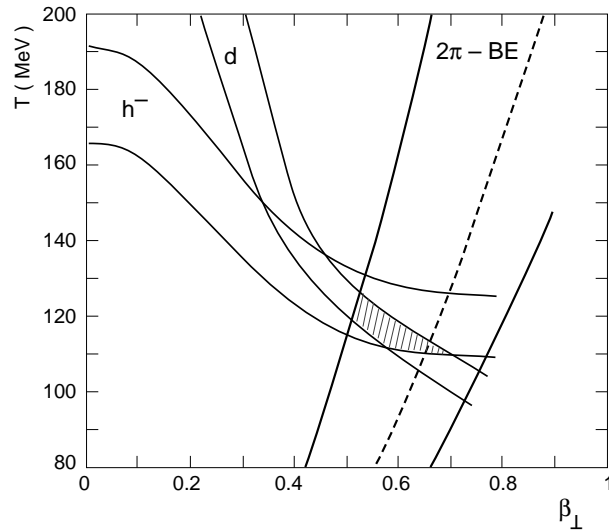
Figure 10: Allowed regions of freeze-out temperature T and transverse flow rapidity η_f (here denoted as $\beta_\perp$) for central Pb+Pb collisions near midrapidity. The bands labelled h^- and d indicate fits to the negative hadron and deuteron spectra; the third band stems from a fit to the sideward radius parameter from 2-pion correlations. (Figure taken with permission from [107].)

A *simultaneous* fit to all the available one- and two-particle distributions was done on Si+Au data from the AGS by Chapman and Nix [63]. They found a freeze-out temperature $T \simeq 90-95$ MeV and an average radial flow velocity of $\langle v_\perp \rangle \simeq 0.34\,c$. A comprehensive analysis of single-particle spectra from Au+Au collisions at the AGS (for which the 2-particle correlations still await publication) confirms [64] the low freeze-out temperature $T \approx 90$ MeV, with an even larger average transverse flow $\langle v_\perp \rangle \approx 0.45\,c$. A preliminary simultaneous analysis of spectra and correlations from Pb+Pb collisions at the SPS measured by NA44 [124] gave $T \sim 95-100$ MeV and $\langle v_\perp \rangle \approx 0.34\,c$. A simultaneous fit to the NA49 Pb+Pb h^- spectra and correlations [125] yielded $T \approx 100$ MeV with $\eta_f = 0.6$, corresponding to an average transverse expansion velocity $\langle v_\perp \rangle \approx 0.5\,c$. These freeze-out temperatures are somewhat lower (and the radial expansion velocity correspondingly higher) than the values extracted from single particle spectra alone [120, 72, 126].

Knowing the average transverse flow velocity $\langle v_\perp \rangle$ and the transverse size R at freeze-out, a lower estimate for the total expansion time can be obtained. Comparing for the Pb+Pb collisions at the SPS the 1-d rms radius at midrapidity, $R \approx 8$ fm (see Sec. 4.5.2), with the corresponding value of a cold Pb nucleus, 3.2 fm, one arrives with $\langle v_\perp \rangle \lesssim 0.5\,c$ at a lower limit of 10 fm/c for the total duration of the transverse expansion. This is larger than the value $\tau_0 \approx 8$ fm/c extracted [107] from the measured midrapidity value of $R_\parallel$ using (46). This illustrates the already mentioned problems of interpreting τ_0 directly as the total expansion time, and it also indicates that the longitudinal expansion was not always boost-invariant, but that the system underwent longitudinal acceleration before freeze-out.

6 GLOBAL TRENDS

6.1 From p+p to Pb+Pb Collisions

Analysis of correlation functions in p+p and π/K+p collisions yields source parameters R of approximately 1 fm [127,128]. Proton collisions upon nuclei yield larger effective sources. As shown above, R_s from p+Pb collisions at 450 GeV is approximately 2 fm, smaller than the corresponding value (3.2 fm) for a cold Pb nucleus. The density of produced particles in such collisions is not large and so significant expansion should not be expected; the increase relative to pp is more likely due to cascading of the struck target nucleons.

In heavy-ion collisions at both AGS and SPS energies significant flow is observed via the $M_\perp$ dependence of the source parameters. Consequently, R_s measured with pairs of finite $M_\perp$ provides only a lower limit to the actual size of the source. Even so, the measured values reflect *effective* sources which are already considerably larger than the initial nuclear overlap region. For Si+Au collisions at 14.6 GeV/nucleon, the ratio ξ of R_s to R_s^{cold} (as defined after Eq. (68)) shows that the source expands by at least a factor $\xi = 1.8$. As their measured correlation functions agreed with those from the RMQD model, the E814 collaboration used RQMD to correct for the flow effects [97]. They inferred an expansion factor $\xi = 2.7$ by comparing $R_t = \sqrt{\langle x^2 + y^2 \rangle}$ from RQMD with the 2-dimensional radius of the projectile in the transverse plane (see Sec. 4.1.5).

For Au+Au collisions at the AGS, the lower limit on the expansion factor from R_s is $\xi \gtrsim 1.6$, while for Pb+Pb at CERN it is $\xi \approx 2$. Data from symmetric collisions of Fe, Nb, and La at the Bevalac [130,129] at 1.3-1.7 GeV/nucleon indicate expansion factors ξ of at least 1.2–1.4.

6.2 Beam Energy Dependence

Central Au+Au collisions at 2, 4, 6, and 8 GeV/A were measured by E895 [99] and analyzed with the parametrizations described in Sec. 2.2.2. Though the analysis is still preliminary, some very interesting trends are evident. The $K_\perp$-dependence of R_s characteristic of radial flow is observed in all but the lowest energy collisions, where pion statistics limit the measurement. Longitudinal flow (via $R_\parallel(K_\perp)$) is seen at all energies. The transverse expansion factor ξ ranges from 1.5 to 2.0. It is intriguing that the *largest* expansion is at the *lowest* energy, where the relative importance of the radial flow appears to be smallest. It is tempting to conclude that lower expansion velocity coupled with large final size implies a long-lived source. However, the data indicate that the emission duration in all cases is quite short, leaving one to wonder why surface emission of pions appears to be missing.

Direct comparisons with Bevalac data are complicated by the inability to select the most central collisions. However, the fits use the function $C(q_\perp, q_\parallel, q^0) = 1 + \lambda \exp[(-q_\perp^2 R_\perp^2 - q_\parallel^2 R_\parallel^2 - (q^0)^2 \tau^2)/2]$, so $R_\perp$ may be compared with R_s. Studies of 1.7 GeV/A Fe+Fe, 1.5 GeV/A Nb+Nb [129] and 1.3 GeV/A La+La collisions [130] yield $R_\perp$ values (corrected by $\sqrt{2}$ for comparison with the AGS fits) of 2.8, 3.4, and 3.2 fm, respectively. These give $\xi = 1.2$–1.4. The disagreement with the low-energy AGS results may be due to the centrality difference of the collisions.

Collecting all of the data together, one may look for trends with $\sqrt{s}$ in the region between 2 and 20 GeV covered by present data. For asymmetric heavy ion

collisions with small projectiles, R_s or $R_\perp$ is always 3-4 fm, regardless of $\sqrt{s}$. For small symmetric systems ($A < 100$), R_s is likewise approximately independent of $\sqrt{s}$, in the range 2.5-3.5 fm. For symmetric systems with $A > 100$, it is more instructive to look at the expansion factor ξ which appears to increase with $\sqrt{s}$. This conclusion relies heavily, however, upon the La+La measurement [130] which is low ($\xi = 1.2$).

7   CONCLUSIONS AND FUTURE PERSPECTIVES

7.1   Where Do We Stand?

In this review we have described the development of a sophisticated framework with which to extract physics from two-particle correlation measurements in heavy-ion collisions. Theoretical and experimental progress in the past decade allows characterization of the particle source in these rather complex systems and gives access, for the first time, to the dynamical evolution. At last the promise of elucidating the space-time evolution of the particle source directly from measured quantities has been realized. These new techniques are now also being applied to e^+e^- collisions.

Two-particle correlations measure collective flow of the matter, via the pair momentum dependence of the homogeneity region, thus fixing the ratio of the freezeout temperature and average flow velocities. Combining this information with an analysis of the single particle spectra uniquely separates temperature and flow. The detailed characterization of the final state which is now possible provides stringent constraints on models simulating the dynamical evolution of the reaction zone.

7.1.1   Heavy-ion collision dynamics

Analysis of correlation functions has shown that tremendous expansion of the system takes place before the hadrons decouple. Longitudinally the source at freeze-out features approximately boost-invariant flow while the transverse dynamics is slightly weaker. Still, the transverse radius of the particle emitting source approximately doubles from initial impact to freeze-out. These features indicate action of a significant pressure, though the hadronic observables are not able to indicate which degrees of freedom are responsible for its build-up.

Already at Bevalac energies, below 2 GeV/nucleon, the hadronic matter expands. However, both the radial flow velocity of the matter and the final source size tend to increase with increasing beam energy. High energy collisions at the SPS result in hadron sources which develop average transverse flow velocities of $0.5\,c$; the hadrons freeze out at temperatures near 100 MeV. Kaons and pions flow together, and the observations are consistent with freeze-out from a common source. From the onset of expansion to freeze-out, the transverse radius increases by a factor of 2.5; given the difference in expansion velocities, the longitudinal growth should be about twice that. The total source volume in Pb+Pb collisions thus grows by a factor of 30!

7.1.2   Initial conditions

The single and two-particle distributions are consistent with formation of a thermalized, flowing hadron gas. The behavior of such a gas may be used to ex-

trapolate back to the early times in the collision, using the *measured* freeze-out conditions and flow gradients constrained by the data. The freeze-out temperature, via the equation of state of an ideal resonance gas, provides an estimate for the local energy density at decoupling (≈ 80 MeV/fm^3 at $T \approx 100$ MeV), the measured transverse flow velocity provides the Lorentz contraction factor γ^2 to correct for the kinetic energy of the expanding matter in the lab frame ($\gamma^2 \approx 1.3$ for $\langle v_\perp \rangle \approx 0.5$). This gives a freeze-out energy density of about 100 MeV/fm^3. With the total expansion factor 30 given above, the initial energy density, at the onset of transverse expansion, should have been of the order of 3 GeV/fm^3, *i.e.* well above the critical energy density $\epsilon_s \lesssim 1$ GeV/fm^3 for color deconfinement as given by lattice calculations [131]. Since the initialization of transverse expansion requires pressure, this large energy density must have been at least partially thermalized. This estimate of the initial energy density (which is averaged over the transverse area of the source) agrees in order of magnitude with simple estimates which use the Bjorken formula [116] with the measured multiplicity density and assume an initial thermalization time $\tau_{\mathrm{eq}} = 1$ fm/c. Compared to the latter it has, however, the advantage that it replaces several features of the highly idealized Bjorken expansion model [116] (e.g. the parameter τ_{eq}) by measured quantities, extracted from the HBT analysis.

7.2   The Future

Experimental measurements in the coming years will develop in several directions. Let us mention a few in which serious activities are already now visible:

7.2.1   Heavy-ion collisions at higher energies

Higher energy collisions (factor of 10 increase in $\sqrt{s}$) will be available at the Relativistic Heavy Ion Collider (RHIC) in late 1999. Experiments will use the techniques described here to map the freeze-out conditions. Quantifying the transverse and longitudinal flow velocities will allow determination of the pressure build-up in the early stages of the collisions. Armed with the extracted velocities, one will be able to back-extrapolate from freeze-out to the time of hadron formation. Full analysis of kaon and proton correlations both extends the accessible $K_\perp$ range and will verify whether these hadrons are emitted from a common source with the pions.

7.2.2   Azimuthally sensitive HBT analysis

We have only discussed the analysis of azimuthally symmetric sources. Even if impact parameter $\boldsymbol{b} = 0$ never occurs, the "central" event ensemble from which the correlation function is constructed is azimuthally symmetric since one averages over the orientation of the collision plane. On the other hand, reconstructing the latter event-by-event opens up an even richer field of activities and phenomena. Azimuthal anisotropies of global event features (in particular directed and elliptic flow, for reviews see [132, 133]) have been studied since the days of the Bevalac, and azimuthally sensitive analyses of single-particle spectra from non-central collisions have recently attracted a lot of attention [134]. The measured elliptic flow of pions and protons at the SPS [135] may play an important role in extracting the pressure in the early collision stage [136]. The next question is how these

azimuthal deformations in momentum-space are correlated with corresponding deformations in coordinate-space. The tools for extracting this information from azimuthally sensitive HBT analyses were developed in [137–139].

Without azimuthal symmetry of the source, the correlator in Gaussian approximation is characterized by 6 functions of 3 variables, see (26). Following the pioneering studies of Voloshin and Cleland [137], it was shown by Wiedemann [138] that for sources whose transverse geometric and dynamical deformations have a dominant quadrupole component this can be reduced to *6 functions of only 2 variables* $(K_\perp, Y)$. The dependence on the angle Φ between $\boldsymbol{K}_\perp$ and the impact parameter $\boldsymbol{b}$ is made explicit in the **Wiedemann parametrization**:

$$
\begin{aligned}
C(\boldsymbol{q}, \boldsymbol{K}) \;=\; & 1 \pm \exp[-R_s^2 q_s^2 - R_o^2 q_o^2 - R_l^2 q_l^2 - 2R_{ol}^2 q_o q_l] \\
& \times \exp[-\alpha_1 \cos\Phi(3q_o^2 + q_s^2) + 2\alpha_1 \sin\Phi q_o q_s] \\
& \times \exp[-\alpha_2 \cos(2\Phi)(q_o^2 - q_s^2) + 2\alpha_2 \sin(2\Phi) q_o q_s]. \quad (70)
\end{aligned}
$$

The parameters R_s, R_o, R_l, R_{ol} are the same as in (27); they are given by the Φ-averages of the corresponding functions of $\boldsymbol{K} = (Y, K_\perp, \Phi)$ in (25) and describe the homogeneity regions of the azimuthally averaged deformed source. The two new parameters $\alpha_{1,2}(K_\perp, Y)$ are related to the first and second harmonic coefficients of R_s in the azimuthal angle Φ. They were shown [138] to characterize dynamic and geometric elliptic anisotropies in the source, respectively.

7.2.3   The average phase-space density at freeze-out

Determination of the phase-space density of particles at freeze-out will be important to check whether the collisions at higher energies produce a source consistent with local thermal equilibrium. It has been speculated that the higher densities of produced particles might cause a pion condensate [7]. Here, a comparison of pion and kaon phase-space densities may be particularly illuminating.

The average phase-space density of pions at freeze-out has already been studied at AGS and SPS energies and found to be consistent with particle emission from a source in local thermal equilibrium. Using Eq. (59), E877 analyzed positive and negative pions from 10.8 A GeV Au+Au collisions near beam rapidity. They found [23] that transverse flow is not needed, and the data are well-described by a thermal source. Study of a compilation [24] of data from S+nucleus and Pb+Pb collisions at the SPS showed a nearly universal behavior of the phase-space density of pions at freeze-out. The data are again consistent with freeze-out from a locally equilibrated source. However, the $p_\perp$-dependence of the spatially averaged phase-space density at mid-rapidity is less steep than that of a Bose-Einstein distribution. Such a deviation is expected due to transverse flow.

7.2.4   Three-pion correlations

Higher order Bose-Einstein correlations will be studied to seek evidence of coherence in the source. An analysis as described in Sec. 2.6 was done by NA44 [140], albeit due to limited statistics only in one dimension. A three-pion correlation function $C_3(q_3) = 1 + \lambda_3 \exp(-R_3^2 Q_3^2)$, with $Q_3^2 = (p_1 - p_2)^2 + (p_2 - p_3)^2 + (p_3 - p_1)^2$, was constructed from central S+Pb collisions at 200 A GeV; it is shown on the left side of Figure 11. The upper dashed line shows the three-pion correlation function expected if the source is totally chaotic and symmetric, while the lower shows the case of vanishing r_3 (see Sec. 2.6). The right side of the Figure shows
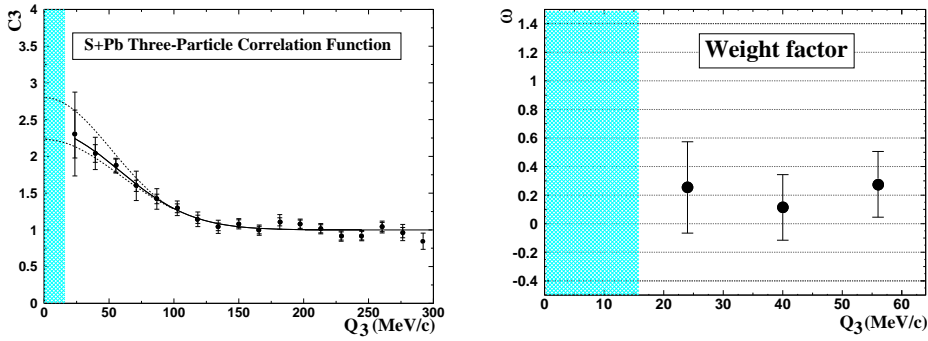
Figure 11: Left panel: Three-pion correlation function from S+Pb collisions measured by NA44, as a function of Q_3 (see text). Right panel: Half the normalized true 3-pion correlator r_3 (here called ω) as a function of Q_3. (Figure taken with permission from [140].)

that the normalized three-pion correlation function r_3 (which is experimentally determined as a weight factor called ω [140]) deviates from 1 in the experiment in the accessible Q_3-range; if this behaviour persisted down to Q_3=0, this would imply partial coherence of the source. It is hoped that the much higher statistics expected at RHIC will settle this important question.

Acknowledgments

Literature Cited

1. Hanbury Brown R, Twiss RQ. *Nature* 178:1046 (1956)
2. Goldhaber G, Goldhaber T, Lee W, Pais A. *Phys. Rev.* 120:300 (1960)
3. Baym G. *Lectures on Quantum Mechanics.* New York: Benjamin (1969)
4. Baym G. *Acta Phys. Pol. B* 29:1839 (1998)
5. Gyulassy M, Kauffmann SK, Wilson LW. *Phys. Rev. C* 20:2267 (1979)
6. Miśkowiec D, Voloshin S. nucl-ex/9704006
7. Pratt S. *Phys. Lett. B* 301:159 (1993); Pratt S, Zelevinsky V. *Phys. Rev. Lett.* 72:816 (1994)
8. Chao WQ, Gao CS, Zhang QH. *J. Phys. G* 21:847 (1995); Zhang QH, Chao WQ, Gao CS. *Phys. Rev. C* 52:2064 (1995)
9. Csörgő T, Zimányi J. *Phys. Rev. Lett.* 80:916 (1998); Zimányi J, Csörgő T. hep-ph/9705432
10. Wiedemann UA. *Phys. Rev. C* 57:3324 (1998)
11. Zhang QH, Scotto P, Heinz U. *Phys. Rev. C* 58:3757 (1998)
12. Shuryak E. *Phys. Lett. B* 44:387 (1973); *Sov. J. Nucl. Phys.* 18:667 (1974)
13. Pratt S. *Phys. Rev. Lett.* 53:1219 (1984); *Phys. Rev. D* 33:1314 (1986)
14. Kolehmainen K, Gyulassy M. *Phys. Lett. B* 180:203 (1986)
15. Padula S, Gyulassy M, Gavin S. *Nucl. Phys. B* 329:357 (1990)
16. Andreev IV, Plümer M, Weiner R. *Int. J. Mod. Phys. A* 8:4577 (1993)

17. Chapman S, Heinz U. *Phys. Lett. B* 340:250 (1994)
18. Heinz U. In *Correlations and Clustering Phenomena in Subatomic Physics*, eds. Harakeh MN, Scholten O, Koch JH. New York: Plenum, NATO ASI Series B 359:137 (1997)
19. Pratt S. In *Quark-Gluon Plasma 2*, ed. Hwa RC. Singapore: Wrld. Sci. (1997), pg. 700
20. Pratt S. *Phys. Rev. C* 56:1095 (1997)
21. Chapman S, Scotto P, Heinz U. *Heavy Ion Physics* 1:1 (1995)
22. Wiedemann UA, Heinz U. *Phys. Rep.* (1999), in press (nucl-th/9901094)
23. Miśkowiec D, et al. *Nucl. Phys. A* 610:227c (1996); Barrette J, et al. (E877 Collaboration). *Phys. Rev. Lett.* 78:2916 (1997)
24. Ferenc D, Heinz U, Tomášik B, Wiedemann UA, Cramer JG. Submitted to *Phys. Lett. B* (hep-ph/9802342)
25. Brown DA, Danielewicz P. *Phys. Lett. B* 398:252 (1997); *Phys. Rev. C* 57:2474 (1998)
26. Koonin SE. *Phys. Lett. B* 70:43 (1977)
27. Baym G, Braun-Munzinger P. *Nucl. Phys. A* 610:286c (1996)
28. Lednický R, Lyuboshitz VL. *Sov. J. Nucl. Phys.* 35:770 (1982); *Heavy Ion Physics* 3:93 (1996); Lednický R, Lyuboshitz VL, Erazmus B, Nouais D. *Phys. Lett. B* 373:30 (1996)
29. Amelin N, Lednický R. *Heavy Ion Physics* 4:241 (1996)
30. Voloshin SA, Lednický R, Panitkin S, Xu N. *Phys. Rev. Lett.* 79:4766 (1997)
31. Soff S, et al. *J. Phys. G* 23:2095 (1997)
32. Miśkowiec D. In *CRIS'98: Measuring the Size of Things in the Universe: HBT Interferometry and Heavy Ion Physics*, eds. S. Costa et al. Singapore: Wrld. Sci. (1999), in press (nucl-ex/9808003)
33. Anchishkin D, Heinz U, Renk P. *Phys. Rev. C* 57:1428 (1998)
34. Sinyukov Yu, Lednický R, Akkelin SV, Pluta J, Erazmus B. *Phys. Lett. B* 432:248 (1998)
35. Barz HW. *Phys. Rev. C* 53:2536 (1996)
36. Chapman S, Scotto P, Heinz U. *Phys. Rev. Lett.* 74:4400 (1995)
37. Chapman S, Nix JR, Heinz U. *Phys. Rev. C* 52:2694 (1995)
38. Akkelin SV, Sinyukov Yu. *Phys. Lett. B* 356:525 (1995)
39. Csörgő T, Lörstad B. *Nucl. Phys. A* 590:465c (1995); Phys. Rev. C 54:1396 (1996)
40. Wiedemann UA, Scotto P, Heinz U. *Phys. Rev. C* 53:918 (1996)
41. Heinz U, Tomášik, Wiedemann UA, Wu YF. *Phys Lett. B* 382:181 (1996)
42. Sinyukov Yu. In *Hot Hadronic Matter: Theory and Experiment*, ed. J. Rafelski. New York: Plenum, NATO ASI Series B 346:309 (1995)
43. Bertsch GF, Gong M, Tohyama M. *Phys. Rev. C* 37:1896 (1988); Bertsch GF, Brown GE. *Phys. Rev. C* 40:1830 (1989)
44. Podgoretskiĭ MI. *Sov. J. Nucl. Phys.* 37:272 (1983)
45. Bertsch GF, Danielewicz P, Herrmann M. *Phys. Rev. C* 49:442 (1994)
46. Herrmann M, Bertsch GF. *Phys. Rev. C* 51:328 (1995)
47. Alber T, et al. (NA35 Collaboration). *Nucl. Phys. A* 590:453c (1995)
48. Chapman S, Scotto P, Heinz U. *Nucl. Phys. A* 590:449c (1995)
49. Heinz U. *Nucl. Phys. A* 610:264c (1996)
50. Tomášik B, Heinz U. *Eur. Phys. J. C* 4:327 (1998)
51. Schlei BR, Strottman D, Xu N. *Phys. Lett. B* 420:1 (1998)
52. Tomášik B. PhD thesis, Universität Regensburg, Jan. 1999
53. Csörgő T, Pratt S. In *Proc. of the Workshop on Relativistic Heavy Ion Collisions at Present and Future Accelerators*, eds. T. Csörgő et al. Budapest: MTA KFKI Press (1991), pg. 75
54. Bertsch GF. *Nucl. Phys. A* 498:173c (1989)
55. Pratt S, Csörgő T, Zimányi J. *Phys. Rev. C* 42:2646 (1990)
56. Fields DE, et al. *Phys. Rev. C* 52:986 (1995)
57. Wu YF, Heinz U, Tomášik B, Wiedemann UA. *Eur. Phys. J. C* 1:599 (1998)
58. Tomášik B, Heinz U. nucl-th/9805016
59. Tomášik B, Heinz U. *Acta Phys. Slov.* (1999), in press (nucl-th/9901006)
60. Yano F, Koonin S. *Phys. Lett. B* 78:556 (1978)
61. Heiselberg H, Vischer A. *Eur. Phys. J. C* 1:593 (1998); *Phys. Lett. B* 421:18 (1998)
62. Gyulassy M, Padula S. *Phys. Lett. B* 217:181 (1988)
63. Chapman S, Nix JR. *Phys. Rev. C* 54:866 (1996); Nix JR. *Phys. Rev. C* 58:2303 (1998)
64. Dobler H. Diploma thesis, Univ. Regensburg, Oct. 1998; Dobler H, Sollfrank J, Heinz U. To be published
65. Abbott T, et al. (E802 Collaboration). *Phys. Rev. C* 50:1024 (1994); Ahle L, et al. (E802

Collaboration). *Nucl. Phys. A* 610:139c (1996); *Phys. Rev. C* 57:R466 (1998); Lacasse R, et al. (E877 Collaboration). *Nucl. Phys. A* 610:153c (1996)

66. Jones PG, et al. (NA49 Collaboration). *Nucl. Phys. A* 610:188c (1996); Appelshäuser H, et al. (NA49 Collaboration). Submitted to *Phys. Rev. Lett.* (NA49 Note number 173)
67. Makhlin AN, Sinyukov YuM. *Z. Phys. C* 39:69 (1988)
68. Kajantie K, Matsui T. *Phys. Lett. B* 164:373 (1985)
69. Bondorf J, Garpman SIA, Zimányi J. *Nucl. Phys. A* 296:320 (1978)
70. Lee KS, Heinz U. *Z. Phys. C* 43:425 (1989); Lee KS, Schnedermann E, Heinz U. *Z. Phys. C* 48:525 (1990)
71. Mayer U, Heinz U. *Phys. Rev. C* 56:439 (1997)
72. Xu N, et al. (NA44 Collaboration). *Nucl. Phys. A* 610:175c (1996); Bearden IG, et al. (NA44 Collaboration). *Phys. Rev. Lett.* 78:2080 (1997)
73. Schlei BR, Ornik U, Plümer M, Weiner RM, *Phys. Lett. B* 293:275 (1992); Bolz J, Ornik U, Plümer M, Schlei BR, Weiner RM. *Phys. Lett. B* 300:404 (1993); *Phys. Rev. D* 47:3860 (1993)
74. Heiselberg H. *Phys. Lett. B* 379:27 (1996)
75. Schlei BR, Ornik U, Plümer M, Strottman D, Weiner RM. *Phys. Lett. B* 376:212 (1996)
76. Csörgő T, Lörstad B, Zimányi J. *Z. Phys. C* 71:491 (1996)
77. Wiedemann UA, Heinz U. *Phys. Rev. C* 56:R610 (1997); *Phys. Rev. C* 56:3265 (1997)
78. Sullivan J, et al. *Phys. Rev. Lett.* 70:3000 (1993)
79. Bertsch GF. *Phys. Rev. Lett.* 72:2349 (1994); *Phys. Rev. Lett.* 77:789(E) (1996)
80. Heinz U, Zhang QH. *Phys. Rev. C* 56:426 (1997)
81. Heiselberg H, Vischer A. nucl-th/9707036
82. Biyajima M, Bartl A, Mizoguchi T, Suzuki N, Terazawa O. *Prog. Theor. Phys.* 84:931 (1990)
83. Plümer M, Razumov LV, Weiner RM. *Phys. Lett. B* 286:335 (1992)
84. Zajc WA. In *Particle Production in Highly Excited Matter*, eds. Gutbrod HH, Rafelski J. New York: Plenum, NATO ASI Series B 303:435 (1992)
85. Csörgő T, et al. *Phys. Lett. B* 241:301 (1990)
86. Sorge H, Stöcker H, Greiner W. *Nucl. Phys. A* 498:567c (1989); *Ann. Phys. (N.Y.)* 192:266 (1989)
87. Alber T, et al. (NA35 Collaboration). *Phys. Rev. Lett.* 74:1303 (1995)
88. Beker H, et al. (NA44 Collaboration). *Phys. Rev. Lett.* 74:3340 (1995)
89. Bearden I, et al. (NA44 Collaboration). *Phys. Rev. C* 58:1656 (1998)
90. Kahana SH, et al. *Phys. Rev. C* 47:R1356 (1993)
91. Rischke D, Gylassy M. *Nucl. Phys. A* 597:701 (1996); *Nucl. Phys. A* 608:479 (1996)
92. Ornik U, Plümer M, Schlei BR, Strottman D, Weiner RM. *Phys. Rev. C* 54:1381 (1996)
93. Schlei BR, Xu N. *Phys. Rev. C* 54:R2155 (1996)
94. Schlei BR. *Heavy Ion Phys.* 5:403 (1997); Schlei BR, Strottman D, Xu N. *Phys. Rev. Lett.* 80:3467 (1998); Schlei BR, Strottman D, Sullivan JP, van Hecke HW. nucl-th/9809070
95. Mattiello R, et al. *Phys. Rev. Lett.* 63:1459 (1989); Sorge H, et al. *Phys. Lett. B* 243:7 (1990)
96. Sorge H, et al. *Phys. Lett. B* 289:6 (1992)
97. Barrette J, et al. (E877 Collaboration). *Phys. Lett B* 333:33 (1994)
98. Baker M. In *Proceedings of the RHIC Winter Workshop 1999*, http://www-rnc.lbl.gov/~nxu/workshop/talk15/
99. Lisa M, et al. (E895 Collaboration). In *Proceedings of the 15th Winter Workshop on Nuclear Dynamics*, ed. W. Bauer: Kluwer Academic Press (1999); to be submitted to *Phys. Rev. Lett.*.
100. Sollfrank J, et al. *Phys. Rev. C* 55:392 (1997); *Heavy Ion Phys.* 5:321 (1997); Huovinen P, Ruuskanen PV, Sollfrank J, *Nucl. Phys. A* 638:503c (1998)
101. Schlei BR, Strottman D. *Phys. Rev. C* 59:R9 (1999)
102. Zajc WA, et al. *Phys. Rev. C* 29 (1984) 2173
103. Bøggild H et al (NA44 Collaboration). *Phys. Lett. B* 302:510 (1993)
104. Beker H, et al. (NA44 Collaboration). *Z. Phys. C* 64:209 (1994)
105. Alber T, et al. (NA35 Collaboration). *Z. Phys. C* 66:77 (1995)
106. Abbott T, et al. (E802 Collaboration). *Phys. Rev. Lett.* 69:1030 (1992)
107. Appelshäuser H, et al. (NA49 Collaboration). *Eur. Phys. J. C* 2:661 (1998)
108. Pratt S, *Phys. Rev. C* 33:72 (1986)

109. Alber T, et al. (NA35 Collaboration). *Z. Phys. C* 73:443 (1996)

110. Akiba Y, et al. (E802 Collaboration). *Phys. Rev. Lett.* 70: 1057 (1993)

111. Cianciolo V, et al. (E859 Collaboration). *Nucl. Phys. A* 590:459c (1995)

112. Gyulassy M, Padula S. *Phys. Rev. C* 41:21 (1990)

113. Nagamiya S. *Phys. Rev. Lett.* 49:1383 (1982)

114. Bøggild H, et al. (NA44 Collaboration). *Phys. Lett B* 349:386 (1995)

115. Bearden IG, et al. (NA44 Collaboration). *Phys. Lett B* 388:431 (1996)

116. Bjorken JD. *Phys. Rev. D* 27:140 (1983)

117. Beavis D, et al. *Phys. Rev. C* 34:757 (1986)

118. Kadija K, et al. (NA49 Collaboration). *Nucl. Phys. A* 610:248c (1996)

119. Lisa M, et al. *Phys. Rev. Lett.* 71:2863 (1993); *Phys. Rev. C* 49:2788 (1994)

120. Braun-Munzinger P, Stachel J, Wessels JP, Xu N. *Phys. Lett. B* 344:43 (1995); *Phys. Lett. B* 365:1 (1996)

121. Csörgő T, Lörstad B, Zimányi J. *Phys. Lett. B* 338:134 (1994)

122. Jacak BV, et al. *Nucl. Phys. A* 590:215c (1995)

123. Wiedemann UA, Tomášik B, Heinz U. *Nucl. Phys. A* 638:475c (1998)

124. van Hecke H, Sullivan JP, Nix JR, Strottman D, Schlei BR. Poster presented at *Quark Matter '97*, see http://p2hp2.lanl.gov/people/hubert/talks/qm97/qm97_index.html

125. Tomášik B. PhD Thesis, Regensburg, 1999; Tomášik B, Wiedemann UA, Heinz U. To be published

126. Kämpfer B, Pavlenko OP, Peshier A, Hentschel M, Soff G. *J. Phys. G* 23:2001 (1997)

127. Lörstad B. *Int. J. Mod. Phys. A* 4:2861 (1988)

128. Agababyan NM, et al. (EHS/NA22 Collaboration). *Phys. Lett. B* 422:359 (1998)

129. Chacon AD, et al. *Phys. Rev. C* 43:2670 (1991)

130. Bossy H, et al. *Phys. Rev. C* 47:1659 (1993)

131. Karsch F. *Nucl. Phys. Proc. Suppl. A* 60:169 (1998)

132. Stöcker H, Greiner W. *Phys. Rep.* 137:277 (1986)

133. Ollitrault JY. *Nucl. Phys. A* 638:195c (1998)

134. Barrette J, et al. (E877 Collaboration). *Phys. Rev. C* 56:3254 (1997); Voloshin S, et al. (E877 Collaboration). *Nucl. Phys. A* 638:455c (1998)

135. Appelshäuser H, et al. (NA49 Collaboration). *Phys. Rev. Lett.* 80:4136 (1998)

136. Sorge H. nucl-th/9812057

137. Voloshin SA, Cleland WE. *Phys. Rev. C* 53:896 (1996); *Phys. Rev. C* 54:3212 (1996)

138. Wiedemann UA. *Phys. Rev. C* 57:266 (1998)

139. Heiselberg H. *Phys. Rev. Lett.* (1999), in press (nucl-th/9809077); Heiselberg H, Levy AM. nucl-th/9812034

140. Bøggild H, et al. (NA44 Collaboration). CERN-EP/99-018